BRAIN
ORIGINAL ARTICLE

The human cognition-enhancing CORD7 mutation increases active zone number and synaptic release

Mila M. Paul,[1,2,†] Sven Dannhäuser,[1,†] Lydia Morris,[3,†] Achmed Mrestani,[1,3,4,†] Martha Hübsch,[1] Jennifer Gehring,[1] Georgios N. Hatzopoulos,[5] Martin Pauli,[1] Genevieve M. Auger,[3] Grit Bornschein,[6] Nicole Scholz,[3] Dmitrij Ljaschenko,[3] Martin Müller,[7] Markus Sauer,[8] Hartmut Schmidt,[6] Robert J. Kittel,[6,9] Aaron DiAntonio,[10] Ioannis Vakonakis,[5,‡] Manfred Heckmann[1] and Tobias Langenhan[3]

[†]These authors contributed equally to this work.

[‡]Present address: Lonza Biologics, Lonza AG, Visp, Switzerland

Humans carrying the CORD7 (cone-rod dystrophy 7) mutation possess increased verbal IQ and working memory. This autosomal dominant syndrome is caused by the single-amino acid R844H exchange (human numbering) located in the 3_{10} helix of the C_2A domain of RIMS1/RIM1 (Rab3-interacting molecule 1). RIM is an evolutionarily conserved multi-domain protein and essential component of presynaptic active zones, which is centrally involved in fast, Ca^{2+}-triggered neurotransmitter release. How the CORD7 mutation affects synaptic function has remained unclear thus far.

Here, we established *Drosophila melanogaster* as a disease model for clarifying the effects of the CORD7 mutation on RIM function and synaptic vesicle release. To this end, using protein expression and X-ray crystallography, we solved the molecular structure of the *Drosophila* C_2A domain at 1.92 Å resolution and by comparison to its mammalian homologue ascertained that the location of the CORD7 mutation is structurally conserved in fly RIM. Further, CRISPR/Cas9-assisted genomic engineering was employed for the generation of *rim* alleles encoding the R915H CORD7 exchange or R915E, R916E substitutions (fly numbering) to effect local charge reversal at the 3_{10} helix. Through electrophysiological characterization by two-electrode voltage clamp and focal recordings we determined that the CORD7 mutation exerts a semi-dominant rather than a dominant effect on synaptic transmission resulting in faster, more efficient synaptic release and increased size of the readily releasable pool but decreased sensitivity for the fast calcium chelator BAPTA. In addition, the *rim* CORD7 allele increased the number of presynaptic active zones but left their nanoscopic organization unperturbed as revealed by super-resolution microscopy of the presynaptic scaffold protein Bruchpilot/ELKS/CAST.

We conclude that the CORD7 mutation leads to tighter release coupling, an increased readily releasable pool size and more release sites thereby promoting more efficient synaptic transmitter release. These results strongly suggest that similar mechanisms may underlie the CORD7 disease phenotype in patients and that enhanced synaptic transmission may contribute to their increased cognitive abilities.

1 Department of Neurophysiology, Institute of Physiology, University of Würzburg, 97070 Würzburg, Germany
2 Department of Orthopaedic Trauma, Hand, Plastic and Reconstructive Surgery, University Hospital of Würzburg, 97080 Würzburg, Germany
3 Division of General Biochemistry, Rudolf Schönheimer Institute of Biochemistry, Medical Faculty, Leipzig University, 04103 Leipzig, Germany

Received July 27, 2021. Revised November 29, 2021. Accepted December 16, 2021. Advance access publication January 12, 2022

4 Department of Neurology, Leipzig University Medical Center, 04103 Leipzig, Germany
5 Department of Biochemistry, University of Oxford, Oxford, OX1 3QU UK
6 Carl Ludwig Institute of Physiology, Medical Faculty, Leipzig University, 04103 Leipzig, Germany
7 Department of Molecular Life Sciences, University of Zürich, 8057 Zürich, Switzerland
8 Department of Biotechnology and Biophysics, University of Würzburg, 97074 Würzburg, Germany
9 Department of Animal Physiology, Institute of Biology, Leipzig University, 04103 Leipzig, Germany
10 Department of Developmental Biology, Washington University School of Medicine, Saint Louis, MO 63110, USA

Correspondence to: Prof. Tobias Langenhan
Division of General Biochemistry
Rudolf Schönheimer Institute of Biochemistry
Medical Faculty, Leipzig University
Johannisallee 30, 04103 Leipzig, Germany
E-mail: tobias.langenhan@gmail.com

Correspondence may also be addressed to: Prof. Manfred Heckmann
Department of Neurophysiology
Institute of Physiology, University of Würzburg
Röntgenring 9, 97070 Würzburg, Germany
E-mail: heckmann@uni-wuerzburg.de

Keywords: CORD7 mutation; active zone; RIM; coupling distance; *d*STORM

Introduction

Presynaptic active zones (AZs) constitute fundamental building blocks of neuronal connections, and contribute to neuronal computation and memory formation.[1–4] They harbour a well-defined set of proteins, which mediate highly regulated neurotransmitter release occurring with sub-millisecond accuracy.[2] Defects in the orchestrated function of presynaptic proteins typically have devastating consequences. Correspondingly, several neurological diseases have been associated with malfunction of presynaptic proteins.[5] A striking exception of the observation that a protein defect leads unambiguously to functional defects is the CORD7 syndrome. Affected individuals suffer from an autosomal dominant cone-rod dystrophy, ultimately leading to blindness.[6] However, they also show largely enhanced cognitive abilities characterized by increased verbal IQ and working memory.[7]

The CORD7 syndrome is caused by a single-amino acid mutation within the 3_{10}-helix of the C_2A domain of RIM (Rab3-interacting molecule).[2,8] RIM is a multi-domain AZ protein,[9,10] encoded by the *RIMS1* locus (human gene name as opposed to the *Drosophila* locus name *rim*), whose interaction with other core AZ proteins such as RIM binding protein (RBP), Munc13, α-Liprin, and ELKS/CAST, as well as with Ca^{2+} channels[2] is thought to figure centrally in neurotransmitter release by providing a structural lattice that organizes release sites. Co-expression with voltage-gated calcium channels in HEK293 cells revealed that the CORD7 exchange in RIM1 increased the activation and suppressed the inactivation component of the channel currents.[11] However, the impact of the CORD7 mutation on synaptic function has remained largely unclear.

At presynaptic release sites, distance between Ca^{2+} channels, vesicular release sensors and the size of the readily releasable pool (RRP) of vesicles are key determinants of the fidelity of neurotransmitter release.[12,13] Tight nanodomain coupling (within tens of nanometres)[12,14,15] promotes fast and efficient release. It can be distinguished from loose coupling,[16–19] but how these differences are molecularly implemented and controlled is still subject of intense investigations.[20–22] Given the central role of RIM at AZs[23] we here studied how RIM, its C_2A domain, and the CORD7 mutation affect synaptic release at the neuromuscular junction (NMJ) of *Drosophila*.

Materials and methods

Fly stocks

Flies and larvae were raised at 25°C on standard cornmeal and molasses medium.

Fly stocks generated in this study

Internal stock IDs given in brackets after the genotype:
w^{1118}; +; $rim^{\Delta C2A}$ *attP DsRed*$^{+}$*/TM3, Sb*; (RIM98)
w^{1118}; +; $rim^{\Delta C2A}$ *attP DsRed*$^{-}$*/TM3, Sb*; (LAT473)
w^{1118}; +; $rim^{\Delta C2A}$ *attP*{C_2A-*WT*(*pLM5*) mW^{-}}*/TM6b, Tb*; (LAT542/AM28)
w^{1118}; +; $rim^{\Delta C2A}$ *attP*{C_2A-*R915H*(*pLM8*) mW^{-}}*/TM6b, Tb*; (LAT545/AM29)
w^{1118}; +; $rim^{\Delta C2A}$ *attP*{C_2A-*R915E,R916E*(*pLM9*) mW^{-}}*/TM6b, Tb*; (LAT549/AM32)
w^{1118}; *P*{*UAS-RIM*^{wt} w^{+}}^{attP40}*/CyoGFP*; +; (RIM52)
w^{1118}; *P*{*UAS-RIM*$^{R>H}$ w^{+}}^{attP40}*/CyoGFP*; +; (RIM53)

Other fly stocks

Reference or stock ID given after the genotype:
w^{1118}; +; rim^{Ex73}; (rim^{KO} allele)[24]
w^{*}; *ok6-GAL4* mW^{+}; +;[25,26]
y^{1} *M{GFP[E.3xP3] = vas-Cas9.RFP-}*$^{ZH-2A}$ w^{1118};;; (BDSC#55821)
M{vas-int.Dm}$^{ZH-2A}$;;;[27]

Transgene construction

Transgenes for genomic targeting

All primer sequences used in this study are provided in Table 1.

pU6-gRNA

CRISPR/Cas9 cutting sites 5′ and 3′ of the genomic region of the *rim/CG33547* gene encoding the C_2A domain were identified by

Table 1 Primer sequences

Primer ID	5′–3′ sequence
lm_30F	ATAGTTTAGCGGCCGCGTTATTCCATGCGCTATATTATAACCACAA
lm_31R	AGGCGCGCCTGTGGGTGTTTTTGGTCCTCTCGCTCTTGT
mh_25F	CTCCGATAGCGCATGGAATAACCTG
mh_26R	AAACCAGGTTATTCCATGCGCTATC
mh_27F	CTCCGAGTCTAATGTATACACGTGT
mh_28R	AAACACACGTGTATACATTAGACTC
mh_46F	CTTCGATAGCGCATGGAATAACCTG
mh_47F	CTTCGAGTCTAATGTATACACGTGT
mh_65F	GTACGCTCTTCCTATCGTGTATACATTAGACTTCAATCG
mh_66R	TAGAGCTCTTCTGACCTTAAATTCGATTTGGGCTCTTAG
mh_77F	ATCTCACCTGCAAGCTCGCACTAGTCGGCGCTCGACAACAGGCAG
mh_79R	GAATCACCTGCAGAACTACGCTAGCGTCTCGCTGGCGGTGGCTCT
mh_82F	TCGCACTAGTCATCCGCAATCCGAACTGTAAACT
mh_83R	CTACGCTAGCCTGTGGAAGTTCCTCAGCTTAGGC
tl_251F	CAACGGCCGACTGCTCGAGGTGACG
tl_252R	AGTCGGCCGTTGAGATCGCAGCGGTGCAGACCCGA
tl_379F	CGCGGATCCATCCCCATCGAGGGACGGCTGCAGC
tl_380R	ATAGTTTAGCGGCCGCCTACTGCAGCTGATACCACTCGGCCTCG
tl_849F	TGGAAGAGCGTGAACAAGTGTGAT
tl_850R	GCTGAGTGCCACTGGAAGTTGGCA
tl_843F	ATTCTACTTCCCGCATACGATG
tl_678R	ATTGAATTAGATCCCGTACGATA
tl_679F	TGTGGTTTGTCCAAACTCATCA
tl_840R	ATGCAATAGTTATCGTTATCGT

CRISPR Optimal Target Finder.[28] The genomic sequence of all CRISPR/Cas9 cleavage sites were confirmed by DNA sequencing of PCR fragments encompassing the suggested sites prior to cloning. Target-specific sequences for gRNAs (gRNA#1: ATAGCGCATGGAATAAC/CTGTGG; gRNA#2: AGTCTAATGTATACACG/TGTGGG; sequences are in 5′–3′ order; the PAM site is underlined, a forward slash indicates the Cas9 cutting site) were synthesized as 5′-phosphorylated oligonucleotides (gRNA#1: mh_46F/mh_26R; gRNA#2: mh_47F/mh_28R), annealed to produce matching overhangs, and ligated into the BbsI sites of the *pU6-BbsI-chiRNA* vector pTL621[29] generating vectors pMH4 (gRNA#1) and pMH5 (gRNA#2).

rim$^{\Delta C2A}$ HDR plasmid

A 1.1 kb fragment encoding the 3′ homology arm was amplified from w^{1118} genomic DNA using primers mh_65F/mh_66R, cut with SapI and inserted into de-phosphorylated SapI-digested pHD-DsRed-attP (pTL620) generating plasmid pMH15. pMH15 was digested with AarI and genomic 0.2 kb PCR product amplified with primers mh_77F/mh_79R, also digested with AarI, were ligated generating plasmid pMH25. Finally, pMH25 was digested with NheI/SpeI and ligated with a 1.1 kb NheI/SpeI-PCR product amplified off genomic DNA with primers mh_82F/mh_83R producing the final HDR vector pMH14.

attB-rim-C_2A^{rescue} plasmid

A 2.5 kb fragment of genomic DNA from strain w^{1118} was amplified using primers lm_30F/lm_31R, digested and ligated to a 6.1 kb NotI/AscI-fragment of pGE-attB-GMR (pTL370) generating *rim-*C_2A^{rescue} vector pLM5.

attB-rim-C_2A^{R915H} plasmid

A 8.5 kb HpaI/XhoI fragment was released from pLM5, and a 0.2 kb HpaI/XhoI fragment from pTL823 (insert synthesized by Genscript). Both fragments were ligated generating *rim-*C_2A^{R915H} vector pLM8.

attB-rim-$C_2A^{R915E,R916E}$ plasmid

A 8.5 kb *HpaI/XhoI* fragment was released from pLM5, and a 0.2 kb HpaI/XhoI fragment from pTL825 (insert synthesized by Genscript). Both fragments were ligated generating *rim-*$C_2A^{R915E,R916E}$ vector pLM9.

UAS transgenes

Plasmids for *Drosophila* transformation were engineered through the *Drosophila* Gateway system as follows. The *Drosophila* wild type full-length *rim* cDNA (GenBank ID: KF534710.1)[24] through a *NotI/XbaI* digest and inserted into the pENTR1Adual plasmid generating entry vector pJG42 (*RIM*^{wt}). Additional entry vectors for single and double mutated RIM variants were produced by exchanging a DNA fragment of pJG42 encoding the CORD7 site region for matching *rim* fragments containing the mutations. These were produced by subcloning the wild-type 0.5 kb *HindIII/NcoI*-fragment of pJG42 into pMCS5 (yielding pTL305) to reduce the plasmid size and allow for an outward PCR of the entire vector. The *rim*$^{R>H}$ mutation was introduced via the reverse outward-PCR primer. The PCR-amplicon was cut at an *EagI* site and self-ligated to recircularize the plasmid. From the resulting clone pTL310 (*RIM*$^{R>H}$) the 0.5 kb *HindIII/NcoI* fragment was used to replace the wild-type region in pJG42 and generate entry vector pTL431. All entry vector inserts were fully sequenced to ensure no errors were introduced through the cloning procedures. To create the final transformation vectors, pJG42 and pTL431 were recombined with the pTW-attB destination vector[27] through an LR reaction according to the manufacturer's instructions (Invitrogen), and correct recombinant clones were identified by suitable restriction digests (*5xUAS-RIM*^{wt} = pTL434; *5xUAS-RIM*$^{R>H}$ = pTL435). All *UAS-RIM* transgenes were inserted into the *attP40* landing site carried on the second chromosome[30] using ΦC31 integrase-based transformation[31] by BestGene Inc.

Transgenes for protein expression

A PCR-amplified DNA fragment encoding the RIM C_2A domain of *Drosophila* (encoding residues 836–962 of RIM) was subcloned via primer-delivered BamHI/NotI sites in a pGEX-6P-2 vector (GE Healthcare) providing a N-terminal GST-tag (pTL423).

CRISPR targeting

All transgenesis steps were performed at Bestgene Inc. For CRISPR/Cas9 mediated engineering *gRNA#1* (pMH4) and *gRNA#2* (pMH5), and the matching *rim*$^{\Delta C2A}$*-HDR* plasmid (pMH14) were injected into *w*^{1118} flies carrying a germline-expressing *vas-Cas9* source as described before[28] producing the *rim*$^{\Delta C2A}$, *DsRed*$^{+}$ allele. Correct gene targeting was confirmed by subsequent sequencing of PCR fragments covering breakpoints between genomic/transgenic DNA amplified off genomic DNA of respective adult transgenic flies using primers tl_843F/tl_687R (covering the 5′ breakpoint), tl_679F/tl_840R (covering the 3′ breakpoint), and across the deleted fragment using primers tl_849F/tl_850R. The 3x*P3-DsRed* transformation marker was removed from *rim*$^{\Delta C2A}$, *DsRed*$^{+}$ flies by expressing a germline Cre source, and confirmed by PCR genotyping. Subsequent insertion of the different *attB-rim-*C_2A transgenes into *rim*$^{\Delta C2A}$, *DsRed*$^{-}$ flies (LAT473) by ΦC31-mediated transgenesis was performed by Bestgene Inc.

Protein production

Recombinant protein expression was performed in *Escherichia coli* strain BL21(DE3) in Luria-Bertani medium. Protein expression was induced at 18°C by addition of 0.3 mM Isopropyl β-D-1-thiogalactopyranoside and allowed to proceed for 16 h. Cell pellets were resuspended in 50 mM Tris-HCl pH 8.0, 250 mM NaCl, 5% v/v glycerol and 3 mM β-mercaptoethanol (β-ME) buffer, and lysed by lysozyme treatment and sonication. Lysates were incubated with Glutathione-sepharose beads (GE Healthcare), and the beads were washed with Buffer A (50 mM Tris-HCl pH 8.0, 250 mM NaCl, 3 mM β-ME). Proteins were eluted from the beads with Buffer A supplemented with 12 mM reduced glutathione, followed by dialysis in Buffer A and removal of the GST-tag by 3C-protease cleavage. Uncleaved proteins and GST were removed by reverse affinity purification with Glutathione-sepharose beads, followed by size exclusion chromatography into a 30 mM sodium citrate pH 6.0, 150 mM NaCl and 1 mM dithiothreitol buffer.

Crystallization and structure determination

Crystals of the *Drosophila melanogaster* RIM C_2A domain were obtained using the sitting drop vapor diffusion technique at 20°C. A Mosquito robot (TTP LabTech) was used to set up 200 nl-size drops with 1:1 and 1.3:0.7 ratios of protein to mother liquor. Rectangular crystals developed in 2 days when mixing the protein at 4.8 mg/ml concentration with a 0.2 M tri-lithium citrate, 20% w/v polyethylene glycol 3350 solution. Crystals and were cryo-protected with 20% v/v glycerol, flash-cooled in liquid nitrogen and diffracted to 1.93 Å at the Diamond Light Source beamline I04. The space group was determined as P212121 with one molecule per asymmetric unit. Crystallographic data were integrated by XDS and scaled in XSCALE.[32] The structure was solved by molecular replacement in the programme MrBump[33] using the rat RIM2 C_2A domain (PDB 2BWQ) as search model. Iterative model building with COOT[34] and refinement in PHENIX.refine[35] using TLS restraints yielded the final model. All figures were prepared in PyMol (PyMOL Molecular Graphics System, Schrödinger LLC). The electrostatics surface potential was calculated with APBS.[36] The structure was deposited under PDB ID 4TS6.

Two-electrode voltage clamp recordings

Two-electrode voltage clamp (TEVC) recordings (Axo Clamp 2B amplifier, Axon instruments) were performed in extracellular haemolymph-like solution (HL-3)[37] that contained (in mM): NaCl 70, KCl 5, $MgCl_2$ 20, $NaHCO_3$ 10, trehalose 5, sucrose 115, HEPES 5, $CaCl_2$ 1.0, pH adjusted to 7.2. Recordings were obtained from NMJs at longitudinal abdominal muscles 6/7 in segments A2 and A3 at 20–22 ± 1°C room temperature using intracellular electrodes with resistances 10–20 MΩ (filled with 3 M KCl). Holding voltage was −60 mV for evoked excitatory postsynaptic currents (eEPSCs) and −80 mV for miniature EPSCs (mEPSCs). Only muscle cells 6 with an initial membrane potential of ≥−50 mV and ≥4 MΩ input resistance were analysed. Synaptic responses were generated by pulses of 0.3 ms length and 5–15 V amplitude, applied via a suction electrode (filled with extracellular solution) and filtered by an 10 kHz low-pass filter. We applied a paired-pulse protocol with 0.2 Hz frequency and 30 ms interpulse intervals, averaged 10 EPSCs per muscle cell if not noted oherwise and analysed the data with Clampfit (Molecular Devices). To estimate RRP size, a train of 50 pulses was applied at 20 Hz. Linear fits to the last 20 pulses were applied to cumulatively plotted eEPSCs and back extrapolated.[38,39]

Focal recordings

EPSC recordings were performed in extracellular haemolymph-like solution (HL-3)[37] that contained (in mM): NaCl 70, KCl 5, $MgCl_2$ 20, $NaHCO_3$ 10, trehalose 5, sucrose 115, HEPES 5, pH adjusted to 7.2 with 1 N NaOH. $CaCl_2$ concentration was 1.0 mM. We only recorded from NMJs at abdominal muscles 6/7 in segments A2 and A3. Room temperature was constantly 20 ± 2°C and temperature of the bath solution was maintained at 20 ± 1°C with the help of a constant displacement pump. The focal electrode (resistances 450–550 kΩ, filled with HL-3) was positioned under optical control on proximal boutons (i.e. nearby the access site of the nerve to the muscle) under optical control. Synaptic currents were low-pass filtered with 20 kHz and stored with Patchmaster software using an EPC10 double patch clamp amplifier (HEKA electronics). EPSCs were evoked by stimulating the respective motor neuron via a suction electrode. We applied a paired pulse protocol at 0.2 Hz with 30 ms interpulse intervals, each pulse consisting of 1 ms length and 7 V amplitude. About 60 traces per recording site were averaged and analysed with Igor Pro 6.05 (Wavemetrics). Rise time was measured from 10% to 90% of the peak eEPSC amplitude and tau decay was fitted from the 50% eEPSC amplitude. Measurement of the synaptic delay was performed as illustrated in the inset of Fig. 3D. BAPTA-AM (Invitrogen) was dissolved in DMSO, which contained 10% Pluronic (F-127, Invitrogen), to create a 10 mM stock solution. Larvae were dissected and incubated for 20 min in 10 µM BAPTA-AM diluted in HL-3 or in Pluronic in DMSO diluted in HL-3 for controls. After incubation, CNS was removed and focal recordings were performed as described above. For fluctuation analysis, focal electrodes with resistances of 1.4–1.8 MΩ were used to record eEPSCs elicited by the paired pulse stimulation protocol described above at bath temperatures of 20 ± 1°C with the help of a constant displacement pump. Approximately 20 traces per recording site and concentration were analysed in consecutive extracellular Ca^{2+} concentrations (0.5, 1.0, 1.5, 3.0, 5.0, 0.5 mM) using Igor Pro 6.37

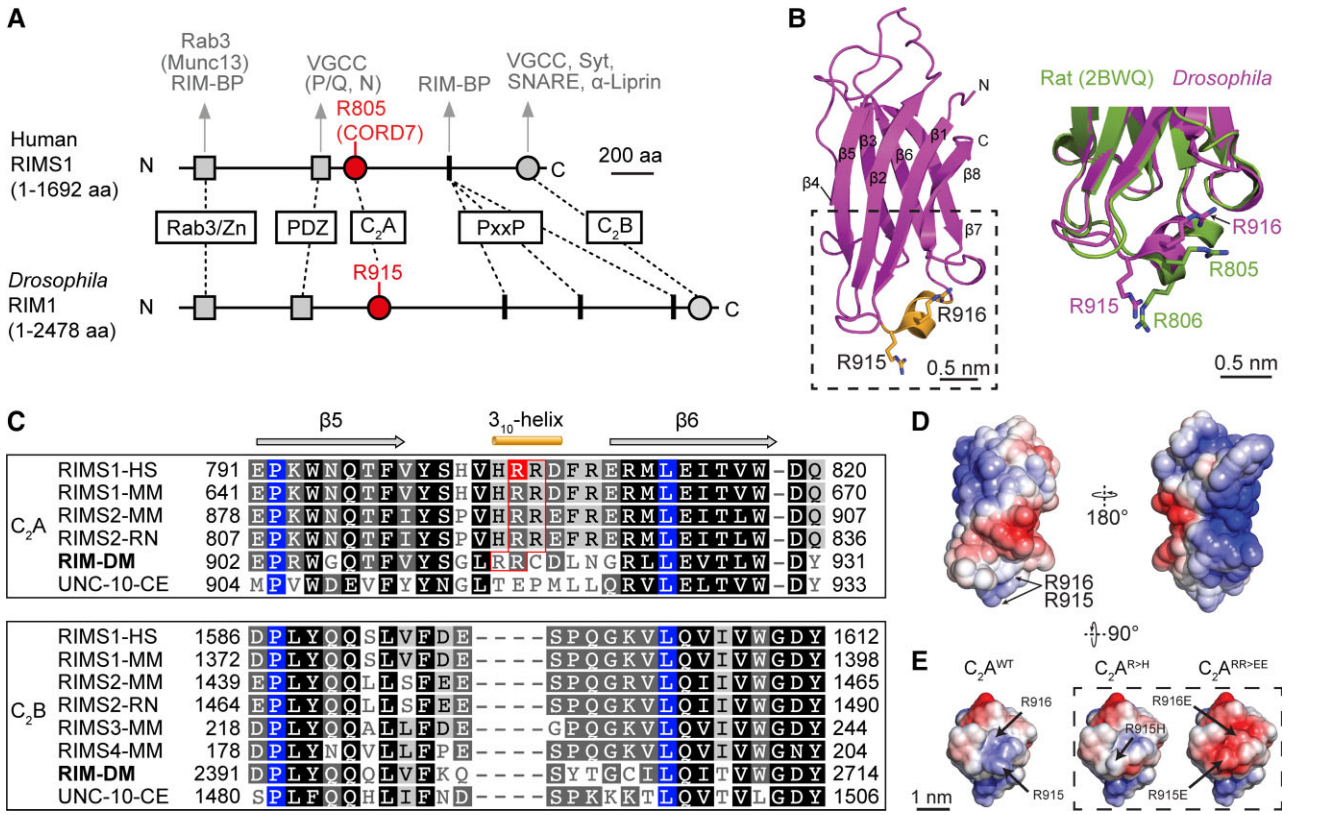

Figure 1 The structure of the RIM C_2A domain is conserved from fly to man. (**A**) RIM protein layout for the human RIMS1 and the *Drosophila* homologue showing the position of its Rab3/Zinc-finger, PDZ, PxxP, C_2A and C_2B domains, known interaction partners are displayed above [the interaction with Munc13 (in parentheses) is observed only in mammals and not *Drosophila*]. Position of the CORD7 mutation site in the C_2A domain (red) is indicated. (**B**) Schematic representation of the *Drosophila* RIM C_2A domain structure. β-strands (β1-β8) are coloured in magenta and the 3_{10}-helix connecting β5 to β6 in yellow. The arginine doublet linked to CORD7 (R915, R916) is shown as sticks. The enlarged view of the dashed box (*right*) shows the superposition of the 3_{10}-helix region of *Drosophila* RIM C_2A (magenta) with rat RIM2 C_2A (green; PDB ID 2BWQ). (**C**) Protein alignments of wild-type RIM C_2A and C_2B domains (truncated for display purpose) from different species. HS = *Homo sapiens*; MM = *Mus musculus*; RN = *Rattus norvegicus*; DM = *Drosophila melanogaster*; CE = *Caenorhabditis elegans*. Alignments for C_2A and C_2B domains were calculated separately. Blue residues correspond to positions that are fully conserved between C_2A and C_2B domains in all displayed RIM homologues. Positions of the 3_{10}-helix (yellow), β-strands 5 and 6 (grey) of the *Drosophila* domain and the CORD7 mutation site in human (red) as part of an RR-motif are denoted. Note that the 3_{10}-helix with the arginine doublet is absent from RIM C_2B domains. GenBank/Uniprot entries: Q86UR5 (RIMS1-HS), Q99NE5 (RIMS1-MM), Q9EQZ7 (RIMS2-MM), Q80U57 (RIMS3-MM), P60191 (RIMS4-MM), AF199329 (RIM2-RN), V5M054 (RIM-DM), Q22366 (UNC-10-CE). (**D**) Electrostatic potential of accessible surfaces for the *Drosophila* RIM C_2A domain. Blue indicates positively charged regions, red negatively charged and white regions without charge. (**E**) Magnification of the domain bottom face in the wild-type, the CORD7 mutation and the RR > EE variants. See also Supplementary Table 1.

(Wavemetrics). eEPSC variances and the variance of the variances were calculated according to Neher and colleagues[40–42] as described previously.[15,38] Variance-mean amplitude plots were fitted using the formula $Var(I) = I/N + qI$, with I meaning the mean eEPSC amplitude, q quantal size and N the number of release-ready vesicles. The release probability P_r for each concentration was calculated as $P_r = I/(Nq)$.

Ca^{2+} imaging

Ca^{2+} imaging was performed in principle as described previously.[43,44] Male wandering third-instar larvae were dissected in ice-cold, Ca^{2+} free HL-3 and incubated in 5 mM Oregon-Green BAPTA-1 488 (Invitrogen) and 1 mM Alexa Fluor568 (Invitrogen) in HL-3 on ice for 10 min. After incubation, the preparation was washed with HL-3 for 10 min. Synapses were imaged with a Scientifica 2P system. Excitation light (800 nm) from a Tsunami laser was focused onto the NMJ using a 60× dipping objective (Olympus, NA 1.0) and emitted light was detected by 2 PIMS-PMT-20 photomultiplier tubes. Single action-potential evoked spatially averaged Ca^{2+} transients were imaged from proximal type Ib boutons of NMJs on muscles 6/7 in abdominal segments A2 and A3 at 1.0 mM $[Ca^{2+}]_{Ex}$. One to two NMJs per preparation and one to six boutons per NMJ were included into the analysis. Line scans (8–12 per bouton) were made at a frequency of 333 Hz. $\Delta F/F$ describes the fluorescence change following an action potential and was quantified as $[F(t) - F_{baseline})/(F_{baseline} - F_{background}]$.[43] Measurements with $F_{baseline} < 210$ analog/digital (A/D)-values were excluded from analysis.

Immunofluorescence imaging

For all imaging experiments we used NMJs formed on abdominal wall muscles 6/7 in segments A2 and A3 from male, wandering third instar larvae. Larvae were dissected in ice-cold Ca^{2+}-free HL-3, fixed with 4% paraformaldehyde in 0.1 M PBS for 10 min and blocked with PBT (PBS containing 0.05% Triton X-100, Sigma) including 5% natural goat serum (Dianova) for 30 min. Primary antibodies were added for overnight staining at 4°C. After three washing steps with PBS (20 min each), preparations were incubated

with secondary antibodies for 2–4 h at room temperature followed by three washing steps. For quantification of AZs per NMJ, filets were mounted in Vectashield (Vector Laboratories) and images acquired using an Apotome System (Zeiss, Axiovert 200 M Zeiss, objective 63×, NA 1.4, oil). Antibodies were used in the following concentrations: mouse mAb α-Brp^{Nc82} (1:250), goat α-mouse conjugated Alexa Fluor488 (1:250, Invitrogen) and goat α-horseradish peroxidase conjugated Cy3 (α-HRP, 1:250, Jackson Immuno Research). Data were analysed using ImageJ software (NIH) as described previously.[45] Images were maximum-projected. If more than one image per NMJ was collected, the duplicate signal that was acquired in the first image was used for quantification. Prior to analysis, signals from axons and neighbouring synapses as well as obvious background were removed manually with the 'Rectangle' or 'Freehand selection' tools in corresponding Brp and α-HRP images. If axons or neighbouring synapses crossed or touched the NMJ directly, images were excluded from analysis. NMJ area and number of Brp spots per NMJ were quantified in α-HRP and Brp images, respectively, using the 'Analyze Particles' function in 8-bit converted images applying an intensity threshold that was fixed for data that were compared statistically. If necessary images were background-subtracted using the Rolling ball method (radius = 50 pixels, α-HRP data in Fig. 4B). The number of boutons per NMJ was counted manually.

*d*STORM

Super-resolution imaging of *Drosophila* larval NMJs was performed as previously described.[46] In brief, larvae were dissected in HL-3, fixed, blocked and stained as described above. After staining, muscle preparations were incubated in 100 mM mercaptoethylamin (MEA, Sigma-Aldrich) buffer in PBS, pH 7.8–7.9 to allow reversible switching of single fluorophores during data acquisition.[47] Images were acquired using an inverted microscope (Olympus IX-71, 60×, NA 1.45, oil immersion) equipped with a nosepiece-stage (IX2-NPS, Olympus). 647 nm (F-04306-113, MBP Communications Inc.), 644 nm (iBEAM-SMART-640-S, Toptica) and 488 nm (iBEAM-SMART-488-S, Toptica) lasers were used for excitation of Alexa Fluor647/Cy5 and Alexa Fluor488 2, respectively. Laser beams were passed through a clean-up filter (Brightline HC 642/10, Semrock, and ZET 488/10, Chroma, respectively) and two dichroic mirrors (Laser-MUX BS 514-543 and HC-quadband BP, Semrock) onto the probe. The emitted fluorescence was filtered with a quadband-filter (HC-quadband 446/523/600/677, Semrock) and divided onto two cameras (iXon Ultra DU-897-U, Andor) using a dichroic mirror (HC-BS 640 imaging, Semrock). In addition, fluorescence was filtered using a longpass (Edge Basic 635, Semrock) or bandpass filter (Brightline HC 525/50, Semrock) for red and green channels, respectively. Pixel size for the super-resolved red channel was 126 nm. Single fluorophores were localized and high resolution-images were reconstructed with rapid*STORM*[48–51] (www.super-resolution.de). Only fluorescence spots with an A/D count higher than 12 000 photons were analysed (10 nm/pixel sub-pixel binning). Antibodies were used in the following concentrations: mouse mAb α-Brp^{Nc82} (1:2000) and goat α-mouse $F(ab')_2$ fragments (A10534, Invitrogen) labelled with Cy5-NHS (PA15101, GE Healthcare) at a concentration of 5.2×10^{-8} M in *ok6-GAL4 > UAS-RIM^{wt}* and *>UAS-RIM$^{R>H}$* larvae, and mouse mAb α-Brp (nc82; 1:100, Antibody Registry ID: AB_2314866, Developmental Studies Hybridoma Bank) and Alexa Fluor647 labelled secondary $F(ab')_2$ fragments goat α-mouse (1:500, A21237, Thermofisher) in *rim^{rescue}/rim^{rescue}* and *rim$^{R>H}$/rim^{rescue}* larvae. Presynaptic boutons were visualized with Alexa Fluor488 conjugated goat-α-HRP (1:250, Jackson Immuno Research). All example AZs in Fig. 4 are shown in top view (i.e. optical axis perpendicular to the AZ plane).

Localization data were analysed essentially as described previously[52] with custom written Python code (https://www.python.org/, language version 3.6). Rapid*STORM* localization tables were directly loaded and analysed. Regions of interest corresponding to the terminal 6 boutons were masked in the reconstructed, binned images from rapid*STORM* using FIJI. For cluster analysis we used the Python implementation of hierarchical density-based spatial clustering of applications with noise (HDBSCAN).[53,54] Brp clusters were extracted with the combination 400 and 100 for 'minimum cluster size' and 'minimum samples', respectively, in *RIM^{wt}* and *RIM$^{R>H}$* measurements, and 100 and 25 for 'minimum cluster size' and 'minimum samples' in *rim^{rescue}/rim^{rescue}* and *rim$^{R>H}$/rim^{rescue}* measurements. The adjustments were necessary due to multiple changes within the experimental setup between measurements (i.e. microscope hardware, antibody concentrations, type of secondary antibody and conjugated dye). Cluster areas were quantified with 2D alpha shapes using CGAL (Computational Geometry Algorithms Library; https://www.cgal.org) in Python ($\alpha = 800$ nm^2). Exclusion criteria for Brp clusters were area <0.01 µm^2 and >0.1 µm^2, Brp localizations per cluster >8000 and mean localization density per cluster >60 000 localizations per µm^2.

Statistical analyses

Datasets in Figs 2 and 6C and D were analysed with Prism 9 (GraphPad Software) and tested for normal distribution applying a one-sample Kolmogorov-Smirnov test. To compare normally distributed datasets, a one-way ANOVA followed by a *post hoc* pairwise comparison with Tukey's correction was applied. Data that were not distributed normally were compared with a Kruskal-Wallis test followed by pairwise comparison with Dunn's analysis. Analyses in Figs 3–5 and Supplementary material were performed with Sigma Plot 12 (Systat Software) using a parametric *t*-test or a non-parametric Mann-Whitney rank sum test depending on data distribution assessed through Kolmogorov-Smirnov testing. For multiple comparisons in Fig. 6A and B, a one-way ANOVA was used. Data are reported as mean ± standard error of the mean (SEM) or median (25th–75th percentile). In box plots, horizontal lines represent median; boxes quartiles; whiskers 10th and 90th percentiles; scatter plots show individual data-points. Whisker plots in Fig. 6D show mean ± SEM.

Data availability

The authors confirm that the data supporting the findings of this study are available within the article and its Supplementary material.

Results

RIM and the structure of the C2A domain are evolutionarily conserved

RIM is a multidomain molecule containing five evolutionarily conserved protein motifs (Fig. 1A)[55] that interact with P/Q- and N-type voltage gated calcium channels (VGCC; through the PDZ and C_2B domains),[56,57] Rab3 (through the Zinc finger domain),[55] other AZ scaffolding partners including ELKS (PDZ domain),[58,59] RBP (Zinc finger domain and PxxP-motif),[60] Synaptotagmin and α-Liprin (C_2B domain),[10] and the presynaptic target membrane.[61] This domain

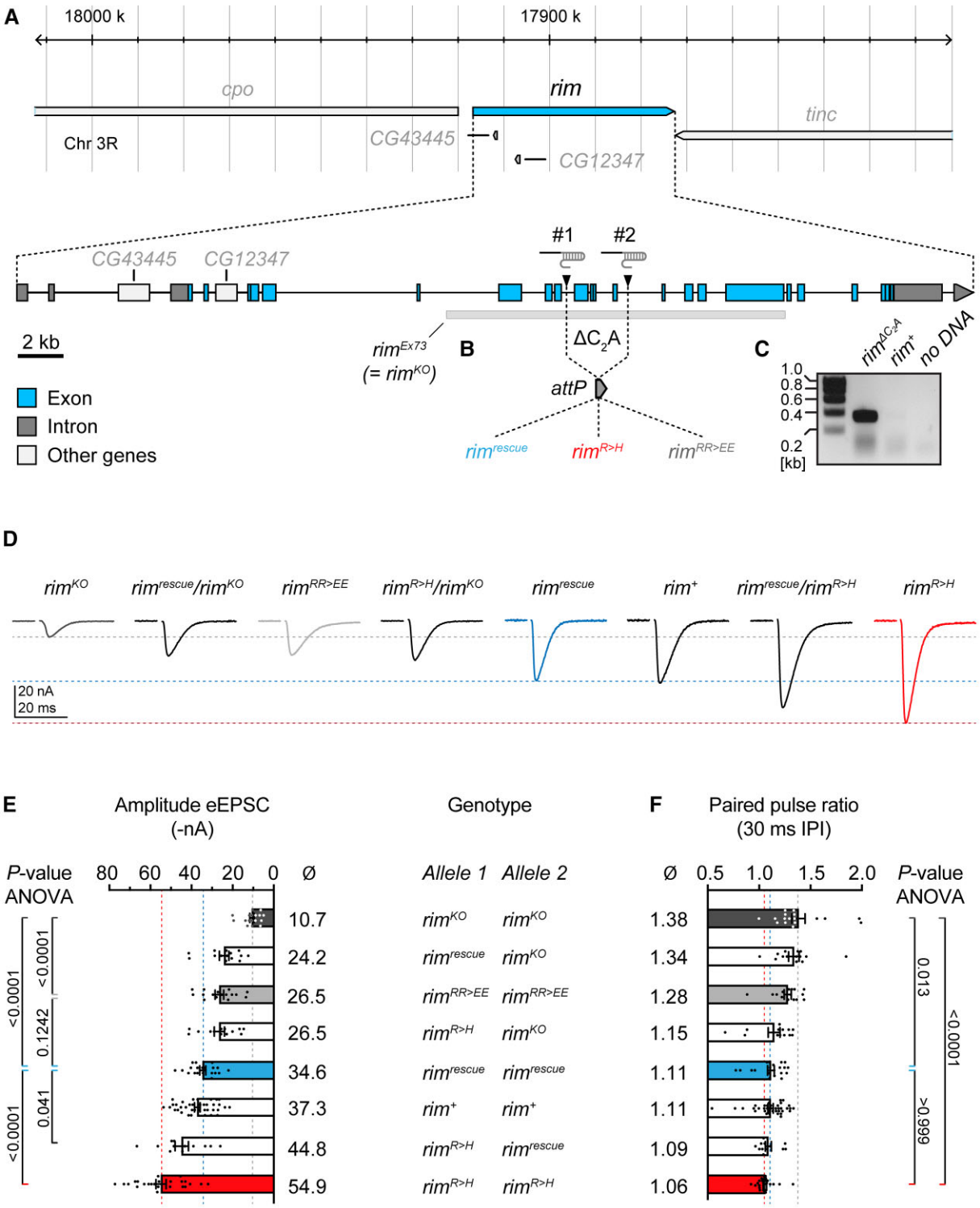

Figure 2 Construction and effect of the *rim*$^{R>H}$ CORD7 allele. (**A**) Overview, gene structure and genomic targeting strategy of the *rim* locus on chromosome III. The position of the *gRNA* probes are marked by #1 and #2, the grey bar denotes the extent of the *rim*^{Ex73} excision[24] used as a *rim*^{KO} null allele in this study. (**B**) Location and size of the *rim* gene fragment excised by CRISPR/Cas9 and replaced by phiC31 integration to generate *rim*^{rescue} (blue), *rim*$^{R>H}$ (red) and *rim*$^{RR>EE}$ (light grey) alleles. (**C**) PCR genotyping confirming the generation of *rim*$^{\Delta C2A}$ allele that allowed for subsequent C_2A domain engineering. (**D**) Representative eEPSC recordings of indicated *rim* genotypes showing the semi-dominant character of CORD7 mutation. (**E** and **F**) Summary graphs and mean values for peak synaptic current amplitudes (**E**) and PPRs (**F**) for indicated *rim* genotypes (*rim*^{KO}/*rim*^{KO}: $n = 17$ NMJs from eight animals; *rim*^{KO}/*rim*^{rescue}: $n = 14$ NMJs from five animals; *rim*$^{RR>EE}$/*rim*$^{RR>EE}$: $n = 16$ NMJs from eight animals; *rim*^{KO}/*rim*$^{R>H}$: $n = 13$ NMJs from six animals; *rim*^{rescue}/*rim*^{rescue}: $n = 20$ NMJs from 13 animals; *rim*$^{+}$/*rim*$^{+}$: $n = 37$ NMJs from 22 animals; *rim*$^{R>H}$/*rim*^{rescue}: $n = 12$ NMJs from six animals; *rim*$^{R>H}$/*rim*$^{R>H}$: $n = 24$ NMJs from 17 animals). See also Supplementary Table 2 for all descriptive statistics and group-by-group statistical comparisons of TEVC and PPR datasets. IPI = interpulse interval.

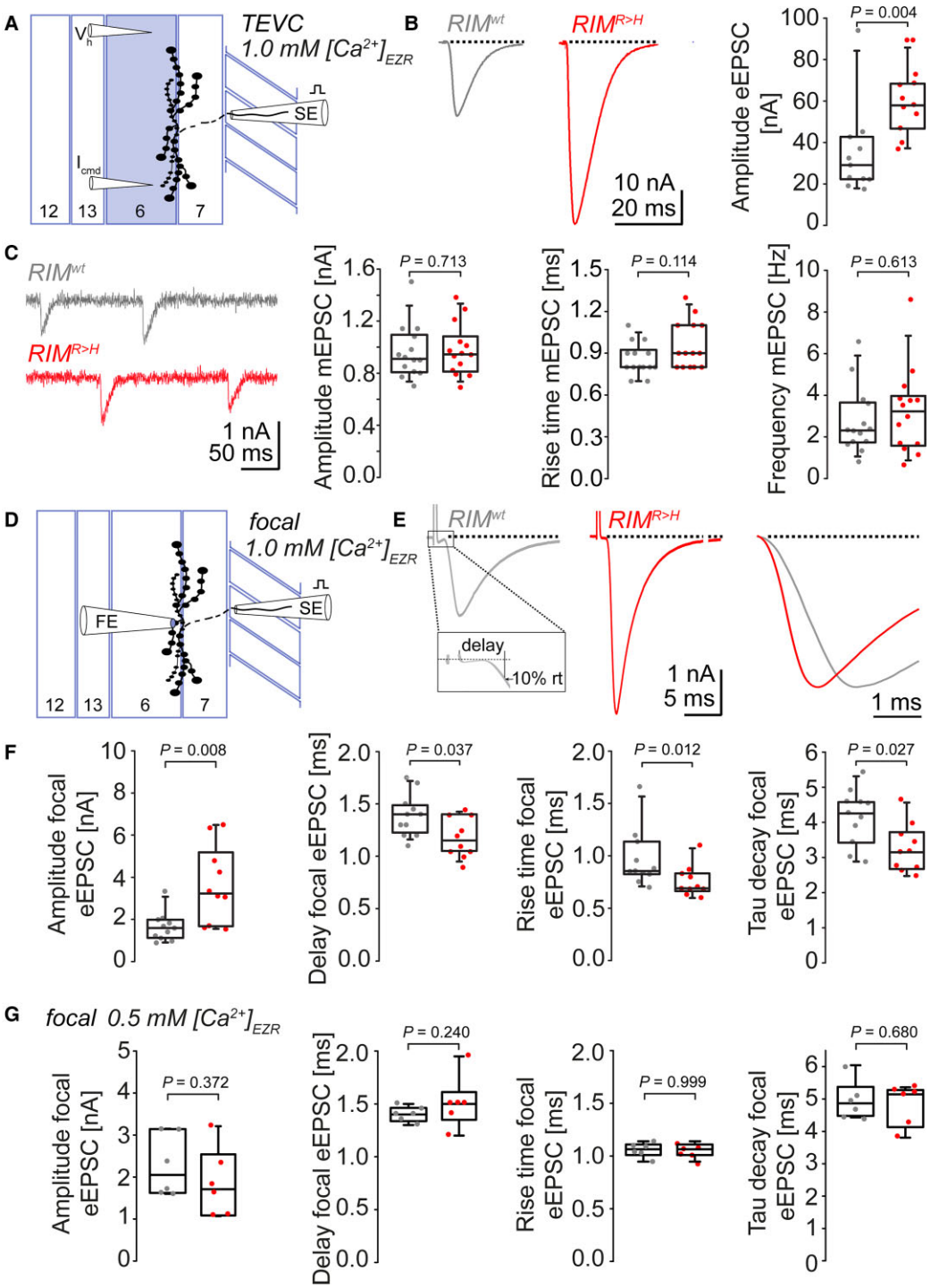

Figure 3 Motor neuron-specific expression of $RIM^{R>H}$ increases and accelerates evoked synaptic currents. (**A**) TEVC recording configuration from *Drosophila* abdominal wall muscle 6 (blue). Action potentials were elicited via motor neuron stimulation using a suction electrode (SE). (**B**) Averaged eEPSCs ($n_{eEPSC} = 20$ per experiment) measured with TEVC at NMJs expressing RIM^{wt} (grey) and $RIM^{R>H}$ (red) under *ok6-GAL4* control and summary graph for eEPSC amplitudes ($n = 11$ NMJs from 11 animals, respectively). (**C**) Example spontaneous mEPSCs and summary graphs for mEPSC amplitude, rise time and frequency ($n_{mEPSC} > 100$ per experiment) in RIM^{wt} (grey) and $RIM^{R>H}$ (red; $n = 14$ NMJs from 14 animals, respectively). (**D**) Focal recording configuration from the *Drosophila* NMJ formed on abdominal wall muscles 6/7. As in **A**, action potentials were elicited via motor neuron stimulation using a suction electrode (SE), but postsynaptic currents were recorded using a focal electrode (FE) placed extracellularly on type Ib boutons (larger boutons in **A** and **D**). (**E**) Averaged focally recorded eEPSCs in RIM^{wt} (grey) and $RIM^{R>H}$ (red; $n_{eEPSC} = 60$ per experiment) and *rightmost*, overlay of normalized traces. *Inset* illustrates determination of synaptic delay measured from the end of the stimulation artefact to 10% of the eEPSC rise time. (**F**) Summary graphs for peak synaptic current amplitude, synaptic delay, rise time and tau decay for RIM^{wt} (grey; $n = 11$ NMJs from 11 animals) and $RIM^{R>H}$ (red; 10 NMJs from 10 animals). Horizontal lines in box plots represent median; boxes quartiles; whiskers 10th and 90th percentiles; scatter plots show individual datapoints. *P*-values are indicated above summary graphs. (**G**) Summary graphs for peak synaptic current amplitude, synaptic delay, rise time and tau decay measured in 0.5 mM extracellular Ca^{2+} concentration in RIM^{wt} (grey; $n = 6$ NMJs from three animals) and $RIM^{R>H}$ (red; $n = 6$ NMJs from three animals). *P*-values are indicated above summary graphs. All displayed measurements made with L3 larvae expressing indicated *RIM* variant as *UAS-RIM*^{X} transgene under control of the motor neuron-specific *ok6-GAL4* enhancer. See also Supplementary Table 3.

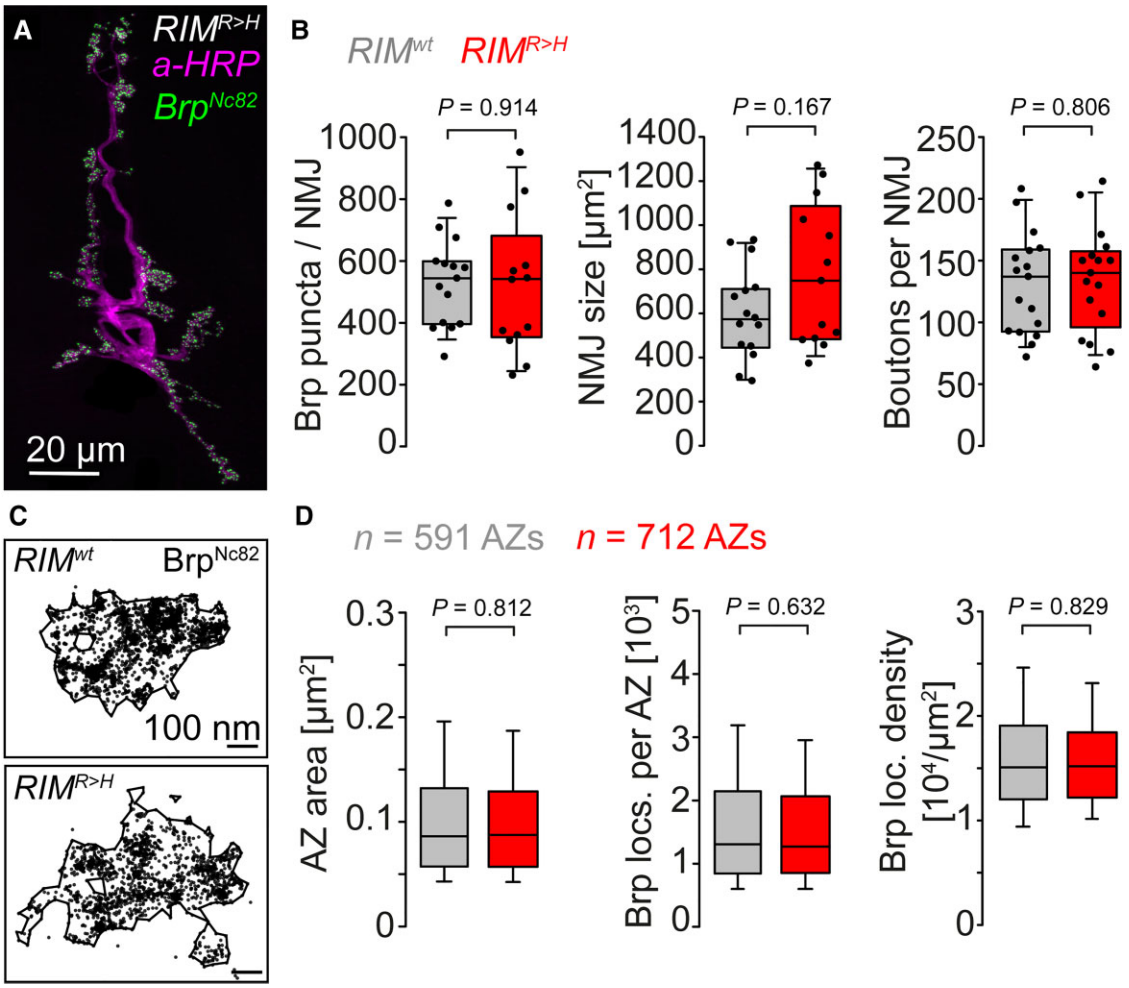

Figure 4 Unchanged AZ number and Brp mesoscale arrangement at $RIM^{R>H}$ NMJs. (**A**) Exemplar *Drosophila* $RIM^{R>H}$ NMJ on abdominal wall muscles 6/7 stained for presynaptic plasma membranes with α-HRP (magenta) and the presynaptic scaffold protein Bruchpilot (Brp^{Nc82}, green). (**B**) Summary graphs for the number of Brp puncta (i.e. considered as 'AZ') per NMJ 6/7 in abdominal segments A2 and A3, NMJ size and the number of boutons per NMJ in RIM^{wt} (grey) and $RIM^{R>H}$ (red; $n = 17$ NMJs from 5 animals, respectively). (**C**) Scatter plot of *d*STORM localizations of individual AZs recognized by Brp^{Nc82} labelled with Cy5 conjugated $F(ab')_2$ fragments in RIM^{wt} and $RIM^{R>H}$. (**D**) Summary graphs for AZ area, the number of Brp localizations (locs.) per individual AZ and Brp localization (loc.) density measured by *d*STORM in RIM^{wt} (grey) and $RIM^{R>H}$ (red; $n = 591$ and 712 AZs from 15 NMJs and four animals, respectively). All displayed measurements made with L3 larvae expressing indicated *RIM* variant as *UAS-RIM*^{X} transgene under control of the motor neuron-specific *ok6-GAL4* enhancer. See also Supplementary Tables 4 and 5.

architecture is already present in invertebrate organisms including *Caenorhabditis elegans* and *Drosophila melanogaster*. RIM C_2A and C_2B domains show considerable homology across different species (Fig. 1C) including over a 3_{10}-helix first observed in structures of the rat homologue that is exposed at the bottom face of the C_2A domain (Fig. 1B). This 3_{10}-helix harbours a missense mutation in a human kindred suffering from cone rod dystrophy type 7 (CORD7), a congenital disease hallmarked by progressive vision loss and increased cognitive abilities.[6,7] The arginine located at the CORD7 site at the N-terminal portion of the 3_{10}-helix is always neighboured by a second arginine forming an RR-motif in all species examined except in the *C. elegans* homologue UNC-10 (Fig. 1C). Interestingly, the CORD7 site corresponds to the first arginine of the RR-motif in vertebrate RIMs but assumes the second position in *Drosophila* on the basis of sequence alignment. Both arginines are likely important for RIM function as they define a distinct positively-charged epitope on the bottom domain surface (Fig. 1D and E).

To determine the effect of the CORD7 mutation on synaptic function it was necessary to confirm that the *Drosophila* RIM C_2A domain also sterically conforms to mammalian homologues. Thus, we recombinantly expressed and crystallized the fly RIM C_2A domain. We obtained a complete diffraction dataset at 1.92 Å resolution (Fig. 1B and Supplementary Table 1), which was used to solve the structure of the fly RIM C_2A domain aided by molecular replacement using the C_2A domain of the rat RIM2 homologue as a model (RIMS2, PDBID: 2BWQ).[8] The final *Drosophila* RIM C_2A model, refined to R/R_{free} of 18.4/21.8%, accounts for residues 836–962 of the protein (Fig. 1B; PDB ID 4TS6). The structure adopts a β-sandwich fold with a small 3_{10}-helix in the loop connecting strands β5-β6, and is highly similar to other C_2 domains having a Cα root-mean-square deviation (RMSD) of just 0.83 Å compared to the rat RIMS2 C_2A variant.[8] Consistent with the sequence alignments, the side chain of the second arginine (R916) in the fly C_2A domain occupies the same position in space as the CORD7 arginine in rat RIMS2 (R805). Interestingly, the side chain of the fly R915 also projects to the same position in space as the rat R806, the C-terminal neighbour of the CORD7 site. Thus, the surface properties of the 3_{10}-helix are highly similar between fly and rat (and presumably human) RIM despite differences in the alignment

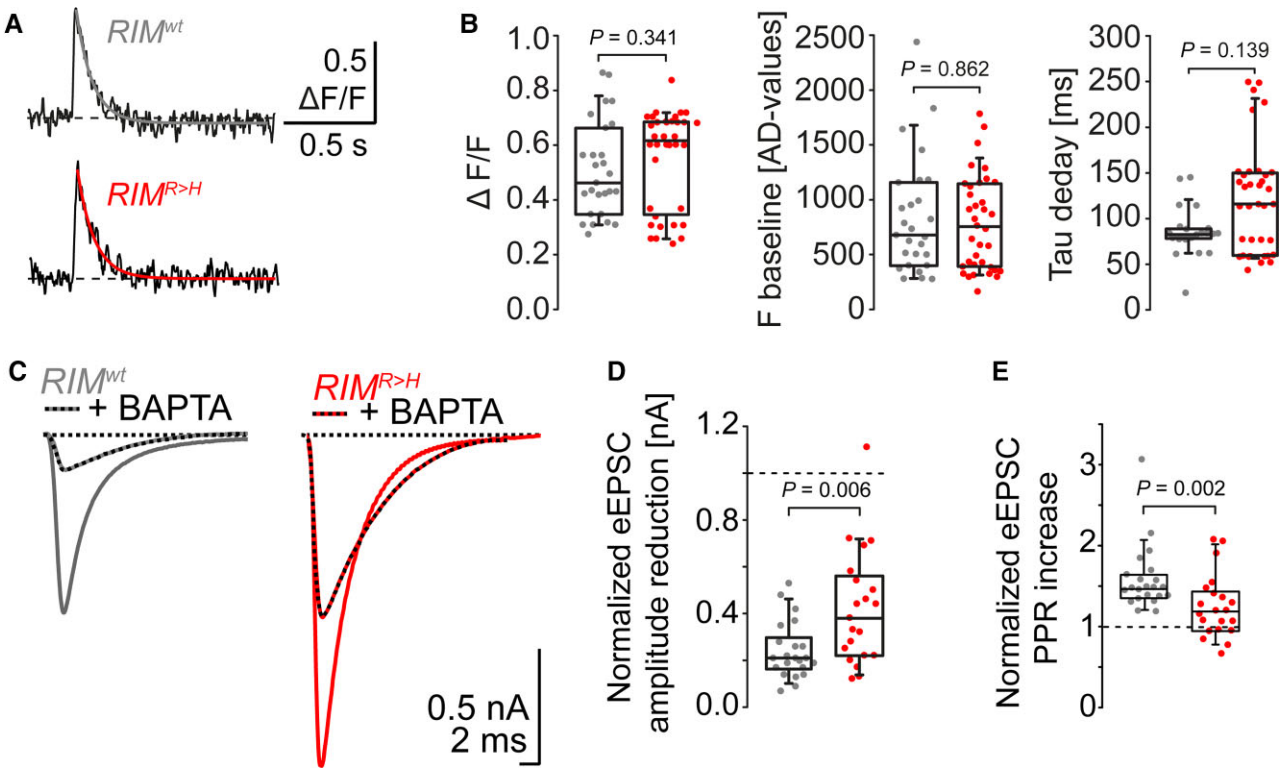

Figure 5 The RIM$^{R>H}$ mutation tightens influx-release coupling while leaving spatially averaged presynaptic Ca^{2+} transients unaffected. (**A**) Representative traces of spatially averaged Ca^{2+} transients in type Ib boutons of *RIM*^{wt} (grey) and *RIM*$^{R>H}$ (red) NMJs (average of 8–12 traces per bouton). (**B**) Summary graphs for peak amplitude (ΔF/F), average baseline fluorescence (F baseline) and tau decay in *RIM*^{wt} ($n = 28$ boutons, 10 NMJs, nine animals) and *RIM*$^{R>H}$ ($n = 36$ boutons, 10 NMJs, seven animals). (**C**) Averaged focally recorded eEPSCs in *RIM*^{wt} (grey) and *RIM*$^{R>H}$ (red; $n_{eEPSC} = 60$ per experiment) before (continuous lines) and after application of BAPTA-AM (dashed lines). (**D** and **E**) Summary graphs for normalized eEPSC amplitude reduction and normalized eEPSC PPR increase induced by BAPTA in *RIM*^{wt} (grey, $n = 22$ experiments from 12 NMJs in six animals for control and BAPTA, respectively) and *RIM*$^{R>H}$ (red, $n = 21$ experiments from 14 and 16 NMJs in seven and six animals for control and BAPTA, respectively). All displayed measurements made with L3 larvae expressing indicated *RIM* variant as *UAS-RIM*^{X} transgene under control of the motor neuron-specific *ok6-GAL4* enhancer. See also Supplementary Table 5.

of the arginine doublet. We suggest that the RR-motif serves the same role in fly and man, as both arginines contribute to the same epitope of the 3_{10}-helix at the bottom face of the RIM C_2A domain.

The RIM CORD7 mutation is a semi-dominant enhancer of synaptic release

To address the functional relevance of the CORD7 mutation in the context of the C_2A domain we employed a CRISPR/Cas9-mediated genomic engineering approach utilizing homology directed repair for genome editing. Through a pair of gRNA probes we removed a 2.5 kb fragment of the *rim* locus that contains the coding region for the C_2A domain (Fig. 2A) and replaced it with an *attP* landing site generating a *rim*$^{\Delta C2A}$ allele (Fig. 2B). Subsequently, this fly strain was used to receive *attB*-flanked transgenes into the *rim* gene through ΦC31 expression (Fig. 2B).[28,62] The transgenes carried the previously removed *rim* gene fragment with either the wild-type C_2A domain sequence (*rim*^{rescue}), a C_2A domain in which the CORD7 mutation was inserted at position R915 (R915H; *rim*$^{R>H}$), or in which the arginine doublet was exchanged for glutamate residues (R915E,R916E; *rim*$^{RR>EE}$). The surface of the 3_{10}-helix of the wild-type RIM C_2A domain appears positively charged (Fig. 1E, C_2A^{WT}). We anticipated that insertion of the CORD7 mutation will slightly alter this electrostatic profile (Fig. 1D) with the surface of the 3_{10}-helix assuming a neutral charge at the site of the CORD7 mutation (Fig. 1E, $C_2A^{R>H}$). In contrast, insertion of negatively charged glutamate residues would result in a pronounced inversion of charge (Fig. 1E, $C_2A^{RR>EE}$) compared to the wild-type situation. All alleles generated through the genomic engineering approach were confirmed through PCR genotyping and sequencing (Fig. 2C). Overt developmental or behavioural abnormalities in animals carrying the different engineered *rim* alleles were not observed.

We first tested the functional consequences of the alleles by TEVC recordings of postsynaptic currents in response to low-frequency nerve stimulation in 1.0 mM extracellular Ca^{2+} at muscle 6/7 neuromuscular junctions of third instar larvae. eEPSCs of *rim*^{rescue} animals (34.6 ± 1.5 nA mean ± SEM throughout this article; Supplementary Table 2 contains all descriptive statistics and results of group-by-group statistical comparisons of all TEVC and PPR datasets) compared indistinguishably to *rim*$^{+}$ control animals (37.3 ± 1.4 nA) that did not undergo the CRISPR/Cas9 genome manipulations demonstrating that our genomic engineering protocol yields precisely constructed *rim* alleles (Fig. 2D and E). We further confirmed that the *rim*^{Ex73} allele[24] behaved as a recessive strong loss-of-function mutation in this assay (*rim*^{KO}: 10.7 ± 1.0 nA; *rim*^{rescue}/*rim*^{KO}: 24.2 ± 2.3 nA). In addition, these results also showed that the wild-type *rim*^{rescue} allele is not completely haplo-sufficient for the eEPSC response as *rim*^{rescue}/*rim*^{KO} heterozygotes displayed significantly lower synaptic responses than *rim*^{rescue} homozygotes (Fig. 2D and E). This indicates that the amount of *rim* gene product is critical for the physiological level of synaptic release.

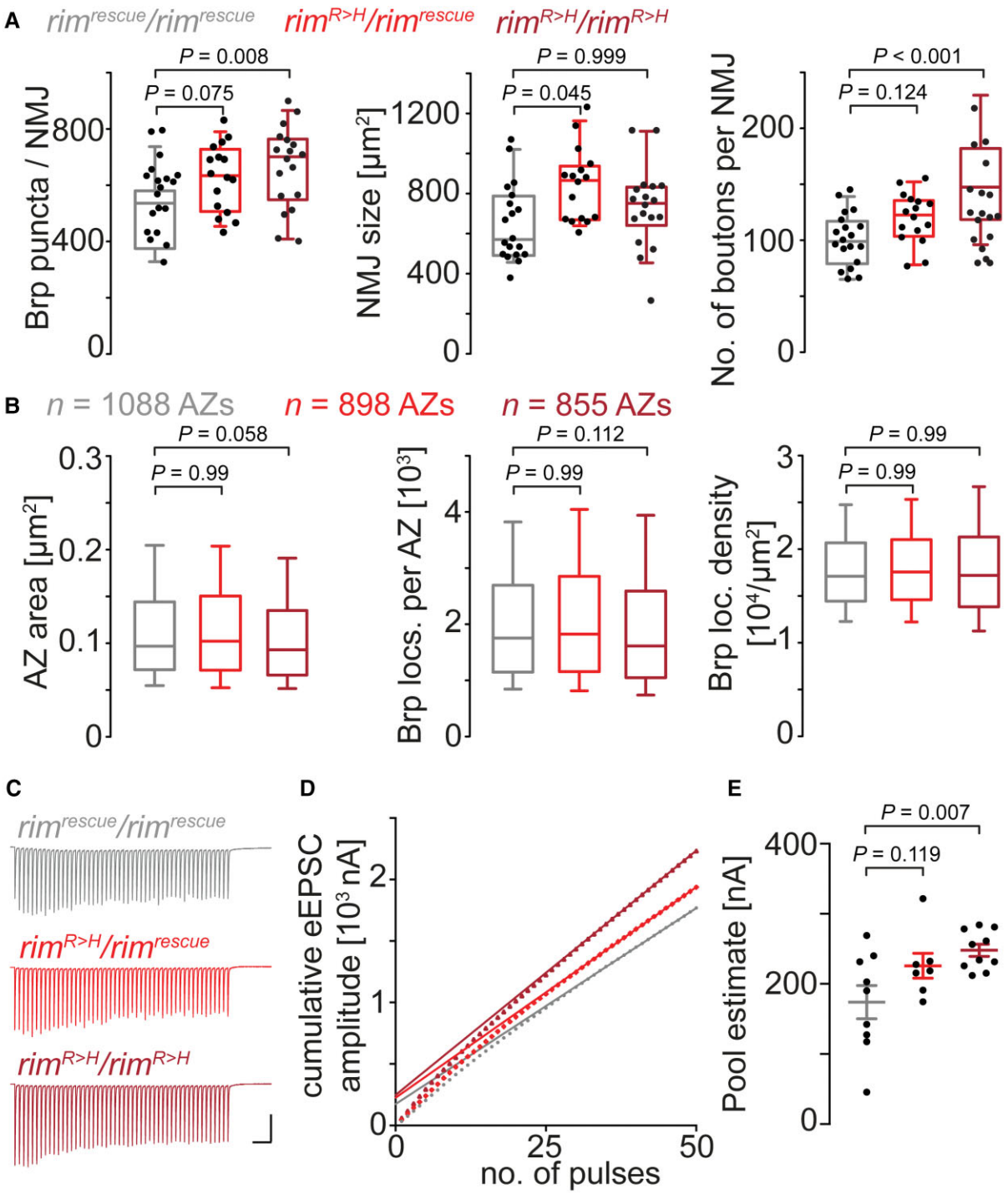

Figure 6 The *rim*$^{R>H}$ CORD7 allele changes NMJ morphology and increases the readily-releasable vesicle pool. (**A**) Summary graphs for the number of Brp puncta per NMJ, NMJ size and the number of boutons per NMJ in *rim*^{rescue}/*rim*^{rescue} (grey), *rim*$^{R>H}$/*rim*^{rescue} (red) and *rim*$^{R>H}$/*rim*$^{R>H}$ (dark red; $n = 19$, 16 and 18 NMJs from seven, seven and six animals, respectively). (**B**) Summary graphs for AZ area, the number of Brp localizations (locs.) per individual AZ and Brp localization (loc.) density measured by *d*STORM *rim*^{rescue}/*rim*^{rescue}, *rim*$^{R>H}$/*rim*^{rescue} and *rim*$^{R>H}$/*rim*$^{R>H}$ ($n = 1088$, 898 and 855 AZs from 17, 17 and 16 NMJs and six, six and six animals, respectively). (**C**) Example eEPSCs in response to 20 Hz trains (50 pulses) in the three genotypes. Scale bars = 200 ms and 20 nA. (**D**) Cumulative eEPSC amplitudes in *rim*^{rescue}/*rim*^{rescue}, *rim*$^{R>H}$/*rim*^{rescue} and *rim*$^{R>H}$/*rim*$^{R>H}$ ($n = 9$, 7 and 10 NMJs and animals, respectively). Back-extrapolation of linear fits to the average cumulative eEPSC amplitude of the last 20 pulses (straight lines) yielded estimates for the readily releasable pool of 174, 226 and 248 for the three genotypes. (**E**) Summary graphs for the estimates of back-extrapolations of the cumulative eEPSC amplitudes in *rim*^{rescue}/*rim*^{rescue}, *rim*$^{R>H}$/*rim*^{rescue} and *rim*$^{R>H}$/*rim*$^{R>H}$. Whisker plots show mean ± SEM, scatter plots individual data-points. All displayed measurements were performed with L3 larvae carrying indicated *rim* alleles (*rim*^{x}/*rim*^{x}). See also Supplementary Tables 6 and 7.

Intriguingly, when we assessed eEPSCs of $rim^{R>H}$ junctions we noticed that homozygous animals carrying the CORD7 mutation in RIM displayed largely increased currents (54.9 ± 2.5 nA; Fig. 2D and E) compared to rim^{rescue} homozygotes. To assess the functional consequences of the $rim^{R>H}$ mutation for synaptic transmission we reduced the $rim^{R>H}$ allele copy number by generating transheterozygous $rim^{R>H}/rim^{rescue}$ animals reflecting the *RIMS1* genotype of CORD7 patients.[6,7] Intriguingly, eEPSC amplitudes of the transheterozygotes ($rim^{R>H}/rim^{rescue}$: 44.8 ± 3.3 nA) settled between the values of the homozygous parents ($rim^{rescue}/rim^{rescue}$ and $rim^{R>H}/rim^{R>H}$) (Fig. 2D and E). In contrast, when $rim^{R>H}$ was placed *in trans* to the *rim* null allele eEPSCs of $rim^{R>H}/rim^{KO}$ animals (26.5 ± 2.5 nA) were indistinguishable from rim^{rescue}/rim^{KO} heterozygotes (24.2 ± 2.3 nA; Fig. 2D and E) showing that CORD7 mutation- carrying $rim^{R>H}$ allele exerts a semi-dominant effect over the rim^{rescue} but not rim^{KO} alleles with regard to eEPSC amplitudes. Collectively, this allelic series uncovered that *rim* gene dosage and the CORD7 change of the C_2A domain of RIM contribute independently to enhanced synaptic release.

Of note, recordings from $rim^{RR>EE}$ larvae showed eEPSCs (26.5 ± 2.1 nA mean ± SEM) that were larger than in rim^{KO} animals but not significantly different from rim^{rescue} and rim^{+} junctions (Fig. 2D and E). This indicates that, in contrast to the CORD7 mutation, the charge reversal at the 3_{10}-helix of RIM's C_2A domain did not profoundly affect eEPSC amplitudes.

Paired-pulse ratio (PPR) measurements confirmed that removal of RIM at rim^{KO} NMJs resulted in facilitation of synaptic release (Fig. 2F and Supplementary Table 2), consistent with previous observations of decreased release probability and strong synaptic facilitation at the NMJ of *rim* hypomorphic *Drosophila* mutants.[43]

To exclude cell non-autonomous effects caused by the germline alteration of *rim* function in engineered $rim^{R>H}$ mutants we next sought to genetically isolate larval motor neurons from an otherwise wild-type nervous system by use of the binary GAL4/UAS expression toolkit. We generated *UAS* transgenes containing either the wild-type *rim* cDNA sequence (RIM^{wt}; in capital letters to contrast this set of transgenes from *rim* alleles) or a cDNA containing the R915H substitution ($RIM^{R>H}$) and expressed them in larval motor neurons by the *ok6-GAL4* driver. The functional consequences of the $RIM^{R>H}$ mutation on synaptic function were tested with TEVC recordings of postsynaptic currents in response to low-frequency nerve stimulation in 1.0 mM extracellular Ca^{2+} (Fig. 3A). eEPSCs in $RIM^{R>H}$ animals were larger than in RIM^{wt} ($RIM^{R>H}$: 59.1 ± 4.5 nA; RIM^{wt}: 35.1 ± 6.5 nA; Fig. 3B and Supplementary Table 3), while mEPSCs and short-term plasticity remained unchanged (Fig. 3C, Supplementary Fig. 1 and Supplementary Table 3) confirming the semi-dominant effect of the $rim^{R>H}$ allele on synaptic release.

While TEVC recordings report the input to an entire muscle cell derived from many boutons, focal electrodes sample from a subset of synaptic boutons with superior temporal resolution (Fig. 3D and Supplementary Table 3). Peak current amplitudes are lower in focal recordings than with TEVC, while they permit resolving synaptic delays and eEPSC rise times. Consistent with results from TEVC focal recordings from proximal type Ib boutons in 1.0 mM extracellular Ca^{2+} revealed that the $RIM^{R>H}$ increases synaptic current amplitudes compared to RIM^{wt} ($RIM^{R>H}$: 3.6 ± 0.6 nA; RIM^{wt}: 1.6 ± 0.2 nA; Fig. 3E and F and Supplementary Table 3). Interestingly, synaptic delay was decreased in $RIM^{R>H}$ (1.18 ± 0.06 ms and 1.39 ± 0.06 ms; Supplementary Table 3) and in addition, rise and decay time were accelerated compared to RIM^{wt} (rise time: 0.75 ± 0.1 ms and 0.97 ± 0.1 ms; tau decay: 3.3 ± 0.2 ms and 4.2 ± 0.2 ms; Supplementary Table 3). However, at lower extracellular Ca^{2+} concentration (0.5 mM) eEPSC amplitudes and kinetics were not changed in $RIM^{R>H}$ (Fig. 3G; amplitude: 2.27 ± 0.74 nA and 1.85 ± 0.81 nA; delay: 1.4 ± 0.07 ms and 1.51 ± 0.25 ms; rise time: 1.06 ± 0.07 ms and 1.06 ± 0.07 ms; tau decay: 4.98 ± 0.59 ms and 4.83 ± 0.64 ms for RIM^{wt} and $RIM^{R>H}$, respectively). This indicates, that the $RIM^{R>H}$ mutation exerts a Ca^{2+}-dependent effect on evoked synaptic release.

Overexpression of $RIM^{R>H}$ leaves synapse and active zone morphology unaltered

To assess whether any of these functional characteristics observed when overexpressing $RIM^{R>H}$ in larval motor neurons are caused by changes of synaptic structure, we performed a morphometric analysis of immunohistochemically processed NMJ preparations. To this end, we focused on the critical AZ scaffold protein Bruchpilot (Brp) and used the highly specific monoclonal antibody Brp^{Nc82}, which recognizes an epitope in the C-terminal part of Brp.[63–65]

We quantified the number of Brp puncta per NMJ in RIM^{wt} and $RIM^{R>H}$ using Brp^{Nc82} and found it indistinguishable between the two groups (Fig. 4A and B and Supplementary Table 4). In addition, the overall NMJ size measured by the extent of the presynaptic α-HRP area and the number of boutons per NMJ were unchanged. Next, to test the impact of the CORD7 mutation on the mesoscale architecture (scale level bridging the nanometer scale of atomic structure and the micrometer scale of cellular ultrastructure)[66] of individual AZs we performed localization microscopy using *d*STORM (direct stochastic optical reconstruction microscopy)[48,50,67] applying a previously approved HDBSCAN analysis.[52] Since Brp is abundantly present at the presynapse and immunolabels by Brp^{Nc82} cover the spatial extent of individual AZs,[46] we equate 'Brp area' with 'AZ area' (Fig. 4C and D). Analysis of AZs in type Ib boutons of the NMJ showed no difference in size or Brp composition of individual AZs between RIM^{wt} and $RIM^{R>H}$ (Fig. 4D and Supplementary Table 4). We conclude that AZ number and synapse morphology as well as the Brp nanoarchitecture are not altered in $RIM^{R>H}$-overexpressing motor neurons.

The CORD7 mutation tightens release coupling

RIM is required for normal levels of presynaptic Ca^{2+} channels[24] and, in addition, the CORD7 mutation was shown to modulate VGCC function.[11] Therefore, we asked whether the $RIM^{R>H}$ mutation affects Ca^{2+} signals at the *Drosophila* NMJ. To test this, we loaded presynaptic terminals with the Ca^{2+} indicator OGB-1 and imaged spatially-averaged Ca^{2+} transients across type Ib boutons in response to single action potential stimulation. We did not observe significant differences in peak amplitudes or decay kinetics of presynaptic Ca^{2+} transients between RIM^{wt} and $RIM^{R>H}$ (Fig. 5A and B and Supplementary Table 5). Thus, the $RIM^{R>H}$ mutation does not affect presynaptic spatially-averaged Ca^{2+} transients, implying unaltered Ca^{2+} influx.

Our data show a striking enhancement of evoked synaptic transmission by the $RIM^{R>H}$ mutation, which requires a yet unnoted mechanistic basis of RIM function since the number of AZs was unchanged at $RIM^{R>H}$ NMJs (Fig. 4B). Tighter coupling causes the release process to be less susceptible to Ca^{2+} chelators, and through nanodomain coupling[20] the slow Ca^{2+} buffer EGTA has little effect at *Drosophila* NMJs.[64] Thus, we loaded presynaptic boutons with the membrane permeable BAPTA-derivative BAPTA-AM (10 µM for 20 min), which results in an intracellular BAPTA concentration in the range of 200–300 µM.[68] We observed a substantial reduction of the measured eEPSC amplitudes in RIM^{wt} (dropping to 24%),

whereas the $RIM^{R>H}$ mutation rendered release less sensitive to BAPTA (dropping to 42%, $P = 0.006$; Fig. 5C–E). These results indicate that the $RIM^{R>H}$ mutation tightens the coupling distance of synaptic vesicles to the calcium source at the AZ.

Allelic $rim^{R>H}$ expression increases the number of presynaptic boutons, active zones and RRP size

So far our analysis revealed striking effects of the RIM CORD7 mutation on synaptic function, which could not be linked to structural synapse alterations in this overexpression situation. However, allelic expression of $rim^{R>H}$ also increased eEPSC amplitudes in TEVC recordings. We wondered whether synaptic morphology was influenced by the CORD7 mutation when expressed under endogenous *cis*-regulatory control. To address this question, we performed immunohistochemical analyses of NMJs 6/7 in $rim^{rescue}/rim^{rescue}$, $rim^{rescue/rimR>H}$ and $rim^{R>H}/rim^{R>H}$ animals using Brp^{Nc82} again as a marker for presynaptic AZs and α-HRP to measure the extent of the presynaptic plasma membrane (Fig. 6). Surprisingly, we found an increased number of AZs and of presynaptic bouton numbers per NMJ as well as enlarged NMJ size due to the $rim^{R>H}$ mutation in a dose-dependent manner (Fig. 6A and Supplementary Table 6). Employing *d*STORM and HDBSCAN algorithms we then analysed the Brp nanoarchitecture in the three genotypes. We found no effect on AZ area, the number of Brp localizations per AZ and Brp localization density in heterozygous $rim^{rescue}/rim^{R>H}$ and homozygous $rim^{R>H}/rim^{R>H}$ variants of the CORD7 mutation (Fig. 6B and Supplementary Table 6). These imaging results suggest that allelic expression of $rim^{R>H}$ changes the overall NMJ morphology without influencing the Brp organization at the mesoscale level.

Finally, we estimated the size of the RRP of synaptic vesicles in animals carrying the $rim^{R>H}$ allele. Through fluctuation analysis of focal recordings we found that q, N and p_r were unchanged (Supplementary Fig. 2). However, linear fits of average cumulative eEPSC amplitudes in response to 20 Hz trains were back-extrapolated to allow estimations for the RRP (Fig. 6C and D). Applying this approach we determined that the RRP size was increased at $rim^{R>H}$ synapses (Fig. 6E and Supplementary Table 7).

Discussion

Protein interactions at presynaptic AZs determine fundamental aspects of neuronal communication. Typically, mutations in proteins are deleterious without ambiguity. A significant exception, however, is a specific mutation in the RIM protein that leads to the CORD7 syndrome.[6] The affected individuals suffer from retinal dystrophy leading to blindness but also show enhanced cognitive capabilities characterized by increases in verbal IQ and working memory.[7] As revealed by large-scale exome sequencing efforts the abundance of the CORD7 mutation in the general human population was found with a minor allele frequency of 0.017% without further indication on putative phenotypes of affected individuals.[69] A thorough analysis of the effects of the CORD7 mutation on neuronal structure or synaptic communication that may ultimately cause the remarkable neurological phenotypes of index family members has thus been warranted.

RIM is a central element of AZs and involved in the configuration of AZ shape, composition and function through multiple protein interactions.[10,11,23,70–72] These roles are at least partially mediated through RIM's domains, which are structurally and biochemically well defined. The clarification of each domain's contribution to synaptic function is complicated through the genetic redundancy of four different *RIMS* loci in addition to the splicing-dependent heterogeneity of their gene products in mammalian model species.[73]

Here we studied the function of the sole *rim* homologue *CG33547* of *Drosophila melanogaster*.[24,43] We first employed X-ray crystallography of the fly RIM C_2A domain to demonstrate that the overall domain layout is strikingly similar and has remained highly conserved throughout evolution. We found that the arginine doublet in the 3_{10}-helix, which is affected in CORD7 patients, is also present in the *Drosophila* C_2A domain and sterically matches the mammalian domain layout.[8] We then analysed the effect of the CORD7 mutation at the *Drosophila* NMJ by genomic engineering of alleles and construction of transgenes with a CORD7-equivalent mutation, and by mimicking the *RIMS1* genotype of CORD7 patients.

Arginine doublets in C_2 domains of AZ proteins, the site at which the CORD7 mutation alters RIMS1's protein structure, have been implicated in different functions and interactions. The arginine doublet of the Synaptotagmin-1 (Syt1) C_2B domain, which is located on the same side of the domain compared to the position of the CORD7 mutation, was previously shown to allow for lipid interaction.[74] This doublet is functionally highly relevant as RR-elimination culminates in release failure and is functionally equivalent to the impairment of calcium binding at the top face of the C_2B domain.[75] In this context the arginine doublet of the C_2B domain appears pertinent for positional priming and site clearance.[76] We found a profound increase of synaptic current amplitudes, and accelerated rise and decay times caused by the CORD7 mutation implying that the $rim^{R>H}$ mutation affects synaptic release at AZs in *Drosophila* too, and thus by analogy also in CORD7 patients. In addition, we found NMJ size and the number of presynaptic AZs per NMJ increased by allelic expression of the CORD7 mutation which might be a contributing factor to release potentiation. Interestingly, also release coupling and changes in RRP size are influenced by the mutation.

The molecular mechanism by which the $rim^{R>H}$ mutation affects synaptic function remains speculative. It was shown that RIM C_2A and C_2B domains interact with the α- and β-subunits of VGCC, SNARE components and synaptotagmins;[10,56,57] one of these interactions may be mediated by the 3_{10}-helix side of the C_2A domain. At the biophysical level $rim^{R>H}$ lessens the positive electrostatic charge found at this site of the wild-type protein and would weaken charge-based interaction forces. However, a weaker electrostatic charge effect of $C_2A^{R>H}$ on this putative target binding may be counteracted by higher hydrophobicity of the histidine amino acid compared to arginine, leading to a net strengthening of this interaction. In contrast, the $rim^{RR>EE}$ substitution not only inverts the charge of this protein site, but it also offers no compensatory hydrophobic effect causing the weakening or disruption of the putative RIM complex. Thus, the $rim^{R>H}$ and $rim^{RR>EE}$ mutations can have opposing molecular effects leading to the observed differences in synaptic response.

Intriguingly, RIM1-mediated modulation of VGCC was altered by the CORD7 mutation *in vitro* displaying impaired function of L-type $Ca_V1.4$, the predominant VGCC that controls release from ribbon synapses in the retina, upon co-expression with $RIMS1^{R>H}$, while calcium conductance through P/Q-type $Ca_V2.1$ channels, which partake in central synaptic release, was augmented.[11,77] These findings offer an explanation for the opposing impact of the CORD7 mutation on the visual and central systems. Our presynaptic calcium indicator measurements argue that the $rim^{R>H}$ mutation does not impact presynaptic Ca^{2+} signals *in vivo*. Instead, enhanced synaptic release in the presence of the CORD7 mutation is likely caused by a reduced coupling distance of synaptic vesicles to the calcium source at the AZ as shown by the reduced effect of a calcium

chelator on eEPSC amplitudes in the presence of $RIM^{R>H}$. This is in line with findings showing that RIM C_2A and C_2B domains interact with the α and β-subunits of VGCC, SNARE components and Synaptotagmins.[11,56,78–80] The RIM-C_2B domain additionally cross-talks with α-Liprin.[10] Rescue experiments of RIM-deficient synapses, however, demonstrate that RIM's capacity to recruit calcium channels to the AZ does not rely on the presence of either C_2 domain, while, in contrast, both C_2 domains facilitate synaptic release without modulating presynaptic calcium channel influx *in vivo*.[23,71] In addition, our investigations revealed an increase of the RRP size at *Drosophila* NMJs. This finding might offer an additional explanation for enhanced synaptic performance in mutants expressing the $rim^{R>H}$ CORD7 allele since RRP enlargement—representing a 'pool engram'—was suggested to be suitable for short-term storage of information.[81] Remarkably, this effect was calcium- and dosage-dependent as measurements in the motor neuron-specific overexpression and the allelic expression revealed. One can speculate that the heterogeneity of evoked synaptic release along the NMJ could contribute to these effects too, thus, employing transgenically expressed GCaMP Ca^{2+} sensors imaging to precisely dissect evoked neurotransmission at different release spots may be a fitting approach to better understand this phenomenon.[82,83] To gain further insight into organization of the synaptic vesicle pool, 3D EM tomographic analyses of vesicle distributions within the presynaptic terminal are attractive.[84] Further investigations are necessary to delineate RIMS1-VGCC interactions and their steric relationship, specifically at retinal and telencephalic mammalian synapses.

A possible cause of the observed release abnormalities at $rim^{R>H}$ synapses is the interference of the mutation with direct molecular interactions, which occur between the 3_{10}-helix of the C_2A domain and yet unknown partners. Alternatively, the CORD7 mutation may impact protein folding and/or stability of the C_2A domain and, thus, the entire RIM molecule. This may result in altered levels of the RIM pool or subcellular localization of RIM at the presynapse and affect neurotransmission. However, the observed gene dosage sensitive gain-of-function effects of $rim^{R>H}$ in direct comparison with loss-of-function alleles ($rim^{RR>EE}$ or rim^{KO}) argue against a reduction or complete depletion of $RIM^{R>H}$ at the synapse. Unfortunately, no α-RIM antibody or transgenically tagged RIM tool is currently available to faithfully assess the amount of RIM protein and its potential change under the influence of the CORD7 mutation.

In sum, the use of the *Drosophila* NMJ as a model system allowed us to uncover the impact of the human CORD7 syndrome mutation of the RIM C_2A domain on speed and efficacy of synaptic release. Future investigations have to detail how the striking cognitive enhancement of CORD7 patients and the functional augmentation of synaptic transmission at *Drosophila* synapses are accomplished through this discrete change in the RIM C_2A domain.

Acknowledgements

We acknowledge the Diamond Light Source for provision of synchrotron radiation facilities and the Helmchen lab for providing access to the Scientifica 2P system. The authors thank P. Jonas for critically reading the manuscript, J. Shiroma for help with protein purification, F. Köhler, M. Oppmann, C. Häusslein and K. Heise for technical assistance, and E. Graf and N. Ehmann for materials and discussions.

Funding

This work was supported by grants from the German Research Foundation (DFG) to M.He., M.S., R.J.K., N.S. and T.L. (SFB-TR166/projects A4, B4, B6, C3; SFB1047/project A5; FOR2149/projects P1 [265903901] and P3 [265996823]; FOR3004 SYNABS/project P1; KI 1460/5-1; LA 2861/7-1), a SNSF Assistant Professor grant (PP00P3-15) and an European Research Council Starting Grant ('SynDegrade', 679881) to M.M., the Biophotonics Initiative of the Bundesministerium for Bildung und Forschung to M.S. (13N11019 and 13N12507) and the IZKF Würzburg to M.M.P. (Z-3/69) and M.He. (N229). I.V. thanks the Wellcome Trust (088497/Z/09/Z) and the Biotechnology and Biological Sciences Research Council UK (BB/J008265/1) for support.

Competing interests

The authors report no competing interests.

Supplementary material

Supplementary material is available at *Brain* online.

References

1. Bailey C, Chen M. Morphological basis of long-term habituation and sensitization in *Aplysia*. *Science*. 1983;220(4592):91–93.
2. Südhof TC. The presynaptic active zone. *Neuron*. 2012;75(1):11–25.
3. Atwood HL, Karunanithi S. Diversification of synaptic strength: presynaptic elements. *Nat Rev Neurosci*. 2002;3(7):497–516.
4. Zhai RG, Bellen HJ. The architecture of the active zone in the presynaptic nerve terminal. *Physiology*. 2004;19(5):262–270.
5. Waites CL, Garner CC. Presynaptic function in health and disease. *Trends Neurosci*. 2011;34(6):326–337.
6. Johnson S, Halford S, Morris AG, *et al*. Genomic organisation and alternative splicing of human RIM1, a gene implicated in autosomal dominant cone-rod dystrophy (CORD7). *Genomics*. 2003;81(3):304–314.
7. Sisodiya SM, Thompson PJ, Need A, *et al*. Genetic enhancement of cognition in a kindred with cone–rod dystrophy due to RIMS1 mutation. *J Med Genet*. 2007;44(6):373–380.
8. Dai H, Tomchick DR, García J, Südhof TC, Machius M, Rizo J. Crystal structure of the RIM2 C_2A-domain at 1.4 Å resolution. *Biochemistry*. 2005;44(41):13533–13542.
9. Castillo PE, Schoch S, Schmitz F, Südhof TC, Malenka RC. RIM1α is required for presynaptic long-term potentiation. *Nature*. 2002;415(6869):327–330.
10. Schoch S, Castillo PE, Jo T, *et al*. RIM1α forms a protein scaffold for regulating neurotransmitter release at the active zone. *Nature*. 2002;415(6869):321–326.
11. Miki T, Kiyonaka S, Uriu Y, *et al*. Mutation associated with an autosomal dominant cone-rod dystrophy CORD7 modifies RIM1-mediated modulation of voltage-dependent Ca^{2+} channels. *Channels*. 2007;1(3):144–147.
12. Adler E, Augustine G, Duffy S, Charlton M. Alien intracellular calcium chelators attenuate neurotransmitter release at the squid giant synapse. *J Neurosci*. 1991;11(6):1496–1507.
13. Neher E. Merits and limitations of vesicle pool models in view of heterogeneous populations of synaptic vesicles. *Neuron*. 2015;87(6):1131–1142.
14. Bucurenciu I, Kulik A, Schwaller B, Frotscher M, Jonas P. Nanodomain coupling between Ca^{2+} channels and Ca^{2+} sensors promotes fast and efficient transmitter release at a cortical GABAergic synapse. *Neuron*. 2008;57(4):536–545.
15. Schmidt H, Brachtendorf S, Arendt O, *et al*. Nanodomain coupling at an excitatory cortical synapse. *Curr Biol*. 2013;23(3):244–249.

16. Vyleta NP, Jonas P. Loose coupling between Ca^{2+} channels and release sensors at a plastic hippocampal synapse. *Science*. 2014;343(6171):665–670.
17. Borst JGG, Sakmann B. Calcium influx and transmitter release in a fast CNS synapse. *Nature*. 1996;383(6599):431–434.
18. Meinrenken CJ, Borst JGG, Sakmann B. Calcium secretion coupling at calyx of held governed by nonuniform channel–vesicle topography. *J Neurosci*. 2002;22(5):1648–1667.
19. Wang LY, Neher E, Taschenberger H. Synaptic vesicles in mature calyx of held synapses sense higher nanodomain calcium concentrations during action potential-evoked glutamate release. *J Neurosci*. 2008;28(53):14450–14458.
20. Eggermann E, Bucurenciu I, Goswami SP, Jonas P. Nanodomain coupling between Ca^{2+} channels and sensors of exocytosis at fast mammalian synapses. *Nat Rev Neurosci*. 2012;13(1):7–21.
21. Yang YM, Fedchyshyn MJ, Grande G, *et al*. Septins regulate developmental switching from microdomain to nanodomain coupling of Ca^{2+} influx to neurotransmitter release at a central synapse. *Neuron*. 2010;67(1):100–115.
22. Kim M, Li G, von Gersdorff H. Single Ca^{2+} channels and exocytosis at sensory synapses. *J Physiol*. 2013;591(13):3167–3178.
23. Kaeser PS, Deng L, Wang Y, *et al*. RIM proteins tether Ca^{2+} channels to presynaptic active zones via a direct PDZ-domain interaction. *Cell*. 2011;144(2):282–295.
24. Graf ER, Valakh V, Wright CM, *et al*. RIM promotes calcium channel accumulation at active zones of the drosophila neuromuscular junction. *J Neurosci*. 2012;32(47):16586–16596.
25. Marqués G, Bao H, Haerry TE, *et al*. The drosophila BMP Type II receptor wishful thinking regulates neuromuscular synapse morphology and function. *Neuron*. 2002;33(4):529–543.
26. Sanyal S. Genomic mapping and expression patterns of C380, OK6 and D42 enhancer trap lines in the larval nervous system of *Drosophila*. *Gene Expr Patterns*. 2009;9(5):371–380.
27. Bischof J, Maeda RK, Hediger M, Karch F, Basler K. An optimized transgenesis system for *Drosophila* using germ-line-specific φC31 integrases. *Proc Natl Acad Sci USA*. 2007;104(9):3312–3317.
28. Gratz SJ, Ukken FP, Rubinstein CD, *et al*. Highly specific and efficient CRISPR/Cas9-catalyzed homology-directed repair in *Drosophila*. *Genetics*. 2014;196(4):961–971.
29. Gratz SJ, Cummings AM, Nguyen JN, *et al*. Genome engineering of *Drosophila* with the CRISPR RNA-guided Cas9 nuclease. *Genetics*. 2013;194(4):1029–1035.
30. Markstein M, Pitsouli C, Villalta C, Celniker SE, Perrimon N. Exploiting position effects and the gypsy retrovirus insulator to engineer precisely expressed transgenes. *Nat Genet*. 2008;40(4):476–483.
31. Groth AC, Fish M, Nusse R, Calos MP. Construction of transgenic *Drosophila* by using the site-specific integrase from phage φC31. *Genetics*. 2004;166(4):1775–1782.
32. Kabsch W. *XDS*. *Acta Crystallogr D Biol Crystallogr*. 2010;66(2):125–132.
33. Keegan RM, Winn MD. *MrBUMP*: an automated pipeline for molecular replacement. *Acta Crystallogr D Biol Crystallogr*. 2008;64(Pt 1):119–124.
34. Emsley P, Cowtan K. *Coot*: model-building tools for molecular graphics. *Acta Crystallogr D Biol Crystallogr*. 2004;60(12):2126–2132.
35. Adams PD, Grosse-Kunstleve RW, Hung LW, *et al*. *PHENIX*: building new software for automated crystallographic structure determination. *Acta Crystallogr D Biol Crystallogr*. 2002;58(11):1948–1954.
36. Baker NA, Sept D, Joseph S, Holst MJ, McCammon JA. Electrostatics of nanosystems: Application to microtubules and the ribosome. *Proc Natl Acad Sci USA*. 2001;98(18):10037–10041.
37. Stewart BA, Atwood HL, Renger JJ, Wang J, Wu CF. Improved stability of *Drosophila* larval neuromuscular preparations in haemolymph-like physiological solutions. *J Comp Physiol*. 1994;175(2):179–191.
38. Weyhersmuller A, Hallermann S, Wagner N, Eilers J. Rapid active zone remodeling during synaptic plasticity. *J Neurosci*. 2011;31(16):6041–6052.
39. Hallermann S, Heckmann M, Kittel RJ. Mechanisms of short-term plasticity at neuromuscular active zones of *Drosophila*. *HFSP J*. 2010;4(2):72–84.
40. Scheuss V, Neher E. Estimating synaptic parameters from mean, variance, and covariance in trains of synaptic responses. *Biophys J*. 2001;81(4):1970–1989.
41. Meyer AC, Neher E, Schneggenburger R. Estimation of quantal size and number of functional active zones at the Calyx of held synapse by nonstationary EPSC variance analysis. *J Neurosci*. 2001;21(20):7889–7900.
42. Scheuss V, Schneggenburger R, Neher E. Separation of presynaptic and postsynaptic contributions to depression by covariance analysis of successive EPSCs at the Calyx of held synapse. *J Neurosci*. 2002;22(3):728–739.
43. Müller M, Liu KSY, Sigrist SJ, Davis GW. RIM controls homeostatic plasticity through modulation of the readily-releasable vesicle pool. *J Neurosci*. 2012;32(47):16574–16585.
44. Wentzel C, Delvendahl I, Sydlik S, Georgiev O, Müller M. Dysbindin links presynaptic proteasome function to homeostatic recruitment of low release probability vesicles. *Nat Commun*. 2018;9(1):267.
45. Paul MM, Pauli M, Ehmann N, *et al*. Bruchpilot and synaptotagmin collaborate to drive rapid glutamate release and active zone differentiation. *Front Cell Neurosci*. 2015;9:29.
46. Ehmann N, van de Linde S, Alon A, *et al*. Quantitative super-resolution imaging of Bruchpilot distinguishes active zone states. *Nat Commun*. 2014;5(1):4650.
47. van de Linde S, Sauer M, Heilemann M. Subdiffraction-resolution fluorescence imaging of proteins in the mitochondrial inner membrane with photoswitchable fluorophores. *J Struct Biol*. 2008;164(3):250–254.
48. Heilemann M, van de Linde S, Schüttpelz M, *et al*. Subdiffraction-resolution fluorescence imaging with conventional fluorescent probes. *Angew Chem Int Ed*. 2008;47(33):6172–6176.
49. Wolter S, Schüttpelz M, Tscherepanow M, van de Linde S, Heilemann M, Sauer M. Real-time computation of subdiffraction-resolution fluorescence images. *J Microsc*. 2010;237(1):12–22.
50. van de Linde S, Löschberger A, Klein T, *et al*. Direct stochastic optical reconstruction microscopy with standard fluorescent probes. *Nat Protoc*. 2011;6(7):991–1009.
51. Wolter S, Löschberger A, Holm T, *et al*. rapidSTORM: accurate, fast open-source software for localization microscopy. *Nat Methods*. 2012;9(11):1040–1041.
52. Mrestani A, Pauli M, Kollmannsberger P, *et al*. Active zone compaction correlates with presynaptic homeostatic potentiation. *Cell Rep*. 2021;37(1):109770.
53. Campello RJGB, Moulavi D, Sander J. Advances in knowledge discovery and data mining, 17th Pacific-Asia conference, PAKDD 2013, Gold Coast, Australia, April 14-17, 2013, Proceedings, Part II. *Lect Notes Comput Sci*. 2013;160–172.
54. McInnes L, Healy J, Astels S. hdbscan: Hierarchical density based clustering. *J Open Source Softw*. 2017;2(11):205.
55. Wang Y, Okamoto M, Schmitz F, Hofmann K, Südhof TC. Rim is a putative Rab3 effector in regulating synaptic-vesicle fusion. *Nature*. 1997;388(6642):593–598.

56. Kiyonaka S, Wakamori M, Miki T, *et al*. RIM1 confers sustained activity and neurotransmitter vesicle anchoring to presynaptic Ca^{2+} channels. *Nat Neurosci*. 2007;10(6):691–701.
57. Han Y, Kaeser PS, Südhof TC, Schneggenburger R. RIM determines Ca^{2+} channel density and vesicle docking at the presynaptic active zone. *Neuron*. 2011;69(2):304–316.
58. Ohtsuka T, Takao-Rikitsu E, Inoue E, *et al*. Cast. *J Cell Biol*. 2002; 158(3):577–590.
59. Wang Y, Liu X, Biederer T, Südhof TC. A family of RIM-binding proteins regulated by alternative splicing: implications for the genesis of synaptic active zones. *Proc Natl Acad Sci USA*. 2002;99-(22):14464–14469.
60. Petzoldt AG, Götz TWB, Driller JH, *et al*. RIM-binding protein couples synaptic vesicle recruitment to release sites. *J Cell Biol*. 2020; 219(7):e201902059.
61. de Jong APH, Roggero CM, Ho MR, *et al*. RIM C2B domains target presynaptic active zone functions to PIP2-containing membranes. *Neuron*. 2018;98(2):335–349.e7.
62. Blanco-Redondo B, Langenhan T. Parallel genomic engineering of two *Drosophila* genes using orthogonal *attB/attP* sites. *G3 (Bethesda)*. 2018;8(9):3109–3118.
63. Wagh DA, Rasse TM, Asan E, *et al*. Bruchpilot, a protein with homology to ELKS/CAST, is required for structural integrity and function of synaptic active zones in *Drosophila*. *Neuron*. 2006;49(6):833–844.
64. Kittel RJ, Wichmann C, Rasse TM, *et al*. Bruchpilot promotes active zone assembly, Ca^{2+} channel clustering, and vesicle release. *Science*. 2006;312(5776):1051–1054.
65. Fouquet W, Owald D, Wichmann C, *et al*. Maturation of active zone assembly by Drosophila Bruchpilot. *J Cell Biol*. 2009;186(1): 129–145.
66. Goodsell DS, Olson AJ, Forli S. Art and science of the cellular mesoscale. *Trends Biochem Sci*. 2020;45(6):472–483.
67. Löschberger A, van de Linde S, Dabauvalle MC, *et al*. Super-resolution imaging visualizes the eightfold symmetry of gp210 proteins around the nuclear pore complex and resolves the central channel with nanometer resolution. *J Cell Sci*. 2012; 125(3):570–575.
68. Baur D, Bornschein G, Althof D, *et al*. Developmental tightening of cerebellar cortical synaptic influx-release coupling. *J Neurosci*. 2015;35(5):1858–1871.
69. Tennessen JA, Bigham AW, O'Connor TD, *et al*. Evolution and functional impact of rare coding variation from deep sequencing of human exomes. *Science*. 2012;337(6090):64–69.
70. Holderith N, Lorincz A, Katona G, *et al*. Release probability of hippocampal glutamatergic terminals scales with the size of the active zone. *Nat Neurosci*. 2012;15(7):988–997.
71. Kaeser PS, Deng L, Fan M, Südhof TC. RIM genes differentially contribute to organizing presynaptic release sites. *Proc Natl Acad Sci USA*. 2012;109(29):11830–11835.
72. Persoon CM, Hoogstraaten RI, Nassal JP, *et al*. The RAB3-RIM pathway is essential for the release of neuromodulators. *Neuron*. 2019;104(6):1065–1080.e12.
73. Wang Y, Südhof TC. Genomic definition of RIM proteins: evolutionary amplification of a family of synaptic regulatory proteins. *Genomics*. 2003;81(2):126–137.
74. Xue M, Ma C, Craig TK, Rosenmund C, Rizo J. The Janus-faced nature of the C2B domain is fundamental for synaptotagmin-1 function. *Nat Struct Mol Biol*. 2008;15(11):1160–1168.
75. Seven AB, Brewer KD, Shi L, Jiang QX, Rizo J. Prevalent mechanism of membrane bridging by synaptotagmin-1. *Proc Natl Acad Sci USA*. 2013;110(34):E3243–E3252.
76. Young SM, Neher E. Synaptotagmin has an essential function in synaptic vesicle positioning for synchronous release in addition to its role as a calcium sensor. *Neuron*. 2009;63(4): 482–496.
77. Dolphin AC. G protein modulation of voltage-gated calcium channels. *Pharmacol Rev*. 2003;55(4):607–627.
78. Takada Y, Hirano M, Kiyonaka S, *et al*. Rab3 interacting molecule 3 mutations associated with autism alter regulation of voltage-dependent Ca^{2+} channels. *Cell Calcium*. 2015;58(3): 296–306.
79. Coppola T, Magnin-Lüthi S, Perret-Menoud V, Gattesco S, Schiavo G, Regazzi R. Direct interaction of the Rab3 effector RIM with Ca^{2+} channels, SNAP-25, and synaptotagmin. *J Biol Chem*. 2001;276(35):32756–32762.
80. Hirano M, Takada Y, Wong CF, *et al*. C-terminal splice variants of P/Q-type Ca^{2+} channel CaV2.1 α1 subunits are differentially regulated by Rab3-interacting molecule proteins. *J Biol Chem*. 2017;292(22):9365–9381.
81. Vandael D, Borges-Merjane C, Zhang X, Jonas P. Short-term plasticity at hippocampal mossy fiber synapses is induced by natural activity patterns and associated with vesicle pool engram formation. *Neuron*. 2020;107(3):509–521.e7.
82. Newman ZL, Hoagland A, Aghi K, *et al*. Input-specific plasticity and homeostasis at the drosophila larval neuromuscular junction. *Neuron*. 2017;93(6):1388–1404.e10.
83. Akbergenova Y, Cunningham KL, Zhang YV, Weiss S, Littleton JT. Characterization of developmental and molecular factors underlying release heterogeneity at *Drosophila* synapses. *Elife*. 2018;7:e38268.
84. Zhan H, Bruckner J, Zhang Z, O'Connor-Giles K. Three-dimensional imaging of *Drosophila* motor synapses reveals ultrastructural organizational patterns. *J Neurogenet*. 2016;30(3–4):237–246.

Supplementary Fig. 1 Short-term plasticity is unchanged by the CORD7 mutation. Related to Figure 3.

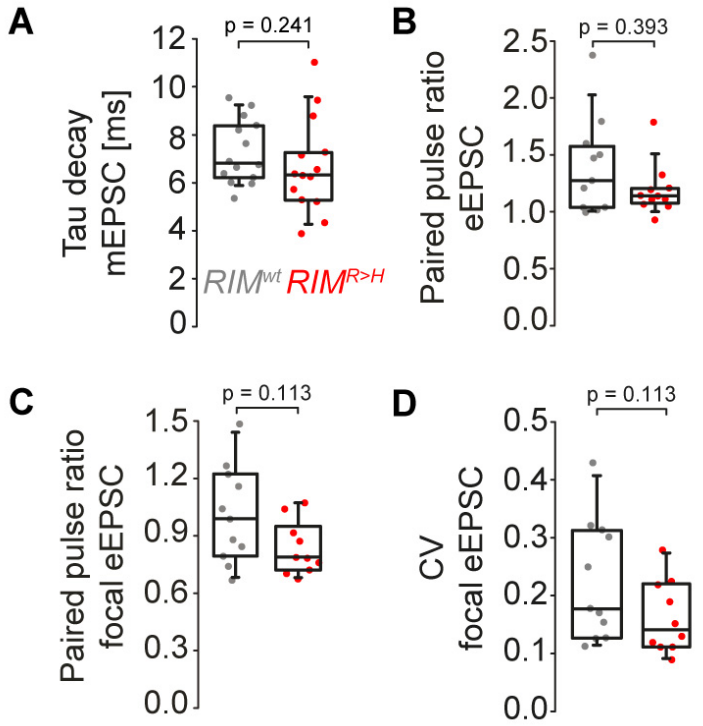

(**A**) Summary graph for mEPSC tau decay (n_{mEPSC} > 100 per experiment) in TEVC recording configuration in *RIM*^{wt} (grey) and *RIM*$^{R>H}$ (red; *n* = 14 experiments and animals, respectively). (**B**) Summary graph for paired pulse ratio measured with TEVC in *RIM*^{wt} (grey) and *RIM*$^{R>H}$ (red; *n* = 11 measurements and animals for each genotype). (**C**) Summary graph for paired pulse ratio and (**D**) coefficient of variation (CV) in focal recordings in *RIM*^{wt} (grey) and *RIM*$^{R>H}$ (red; *n* = 11 and 10 experiments and animals, respectively). Horizontal lines in box plots represent median; boxes quartiles; whiskers 10th and 90th percentiles; scatter plots show individual data points.

All displayed measurements made with L3 larvae expressing indicated *RIM* variant as *UAS-RIM*^{X} transgene under control of the motoneuron-specific *ok6-GAL4* enhancer.

Supplementary Fig. 2 Unchanged *N* and p_r in $rim^{R>H}/rim^{rescue}$. Related to Figure 6.

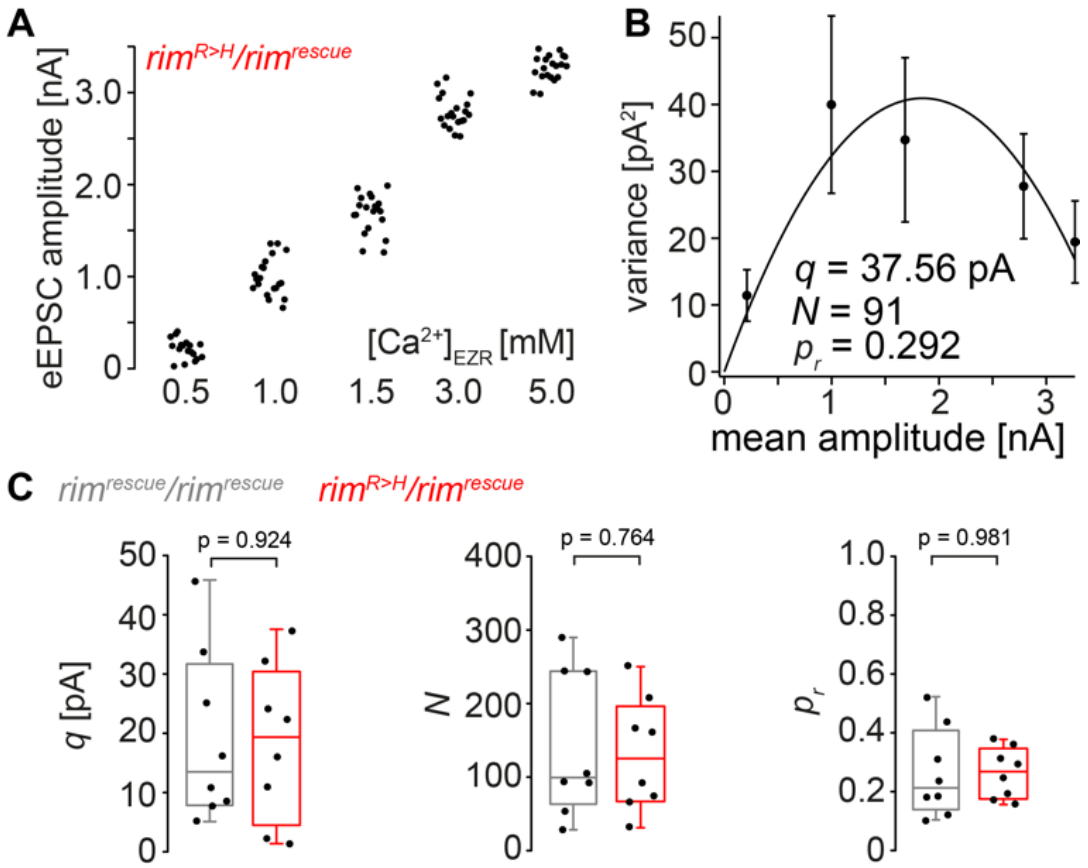

(**A**) Fluctuation analysis of eEPSC amplitudes recorded focally at the indicated extracellular Ca^{2+} concentrations at NMJs 6/7. Example amplitude distribution from a $rim^{R>H}/rim^{rescue}$ animal. (**B**) Variance of the eEPSC amplitudes from (A) plotted against the corresponding amplitude means, error bars indicate variances of the variance. The parabolic fit yields quantal size *q*, the binominal parameter *N* and the release probability p_r. *q*, *N* and p_r at 1 mM extracellular Ca^{2+} for the recording in (**A**) are indicated. (**C**) Summary graphs for *q*, *N* and p_r in $rim^{rescue}/rim^{rescue}$ (grey) and $rim^{R>H}/rim^{rescue}$ (red; n = 8 NMJs from 8 animals, respectively).

All displayed measurements were performed with L3 larvae carrying indicated *rim* alleles (rim^x/rim^x).

Supplementary Table 1 Crystallographic data collection and refinement statistics. Related to Figure 1.

Protein	**DmRIM C_2A**
PDB entry ID	4TS6
Space group	$P\ 2_1\ 2_1\ 2_1$
Unit cell (Å)	a = 32.08; b = 38.70; c = 131.37
Beamline	DLS/I04
Wavelength (Å)	0.9999
Resolution range (Å)	65.68-1.92
High resolution shell (Å)	1.97-1.92
R_{Merge}[a]	0.057 (0.643)
R_{Pim}[a]	0.025 (0.281)
Completeness[a] (%)	99.9 (99.7)
Multiplicity[a]	6.9 (7.1)
I/σ (I)[a]	17.5 (2.8)
Refinement statistics	
R_{work} (reflections)	0.184 (12492)
R_{free}(reflections)	0.218 (648)
Number of atoms	
Protein atoms	1046
Water	89
Average B factors (Å^2)	
Protein atoms	35.4
Water	48.5
RMSD from ideal values	
Bonds / angles (Å/°)	0.008 / 1.22
MolProbity statistics [73]	
Ramachandran favored (%)	98.39
Ramachandran disallowed (%)	0.0
Clashscore (percentile)	1.93 (100%)
MolProbity score (percentile)	0.96 (100%)

[a] Values in parentheses correspond to the high resolution shell

Supplementary Table 2 Data summary and statistical information of TEVC recordings of L3 larvae carrying indicated *rim* alleles. Related to Figure 2.

Genotype	eEPSC amplitude [nA]		PPR (30 ms IPI)	
	mean ± SEM	*P*-value	mean ± SEM	*P*-value
rim^{KO}/rim^{KO} (*n* = 17 NMJs from 8 larvae)	10.67 ± 1.043		1.383 ± 0.065	
vs. rim^{KO}/rim^{rescue}		0.0011		>0.9999
vs. $rim^{R915E.R916E}/rim^{R915E.R916E}$		<0.0001		>0.9999
vs. rim^{KO}/rim^{R915H}		<0.0001		0.6604
vs. $rim^{rescue}/rim^{rescue}$		<0.0001		0.013
vs. rim^{+}/rim^{+}		<0.0001		0.0018
vs. rim^{rescue}/rim^{R915H}		<0.0001		0.0031
vs. rim^{R915H}/rim^{R915H}		<0.0001		<0.0001
rim^{KO}/rim^{rescue} (*n* = 14 NMJs from 5 larvae)	24.17 ± 2.312		1.338 ± 0.051	
vs. $rim^{R915E.R916E}/rim^{R915E.R916E}$		0.9964		>0.9999
vs. rim^{KO}/rim^{R915H}		0.9972		0.809
vs. $rim^{rescue}/rim^{rescue}$		0.0209		0.0238
vs. rim^{+}/rim^{+}		0.0002		0.0049
vs. rim^{rescue}/rim^{R915H}		<0.0001		0.0054
vs. rim^{R915H}/rim^{R915H}		<0.0001		<0.0001
$rim^{R915E.R916E}/rim^{R915E.R916E}$ (*n* = 16 NMJs from 8 larvae)	26.49 ± 2.072		1.278 ± 0.034	
vs. rim^{KO}/rim^{R915H}		>0.9999		>0.9999
vs. $rim^{rescue}/rim^{rescue}$		0.1242		0.0585
vs. rim^{+}/rim^{+}		0.0021		0.0131
vs. rim^{rescue}/rim^{R915H}		<0.0001		0.0131
vs. rim^{R915H}/rim^{R915H}		<0.0001		<0.0001
rim^{KO}/rim^{R915H} (*n* = 13 NMJs from 6 larvae)	26.52 ± 2.500		1.146 ± 0.057	
vs. $rim^{rescue}/rim^{rescue}$		0.1816		>0.9999
vs. rim^{+}/rim^{+}		0.0061		>0.9999
vs. rim^{rescue}/rim^{R915H}		<0.0001		>0.9999
vs. rim^{R915H}/rim^{R915H}		<0.0001		0.2986
$rim^{rescue}/rim^{rescue}$ (*n* = 20 NMJs from 13 larvae)	34.60 ± 1.472		1.114 ± 0.032	
vs. rim^{+}/rim		0.9607		>0.9999
vs. rim^{rescue}/rim^{R915H}		0.041		>0.9999
vs. rim^{R915H}/rim^{R915H}		<0.0001		>0.9999
rim^{+}/rim^{+} (*n* = 37 NMJs from 22 larvae)	37.25 ± 1.383		1.112 ± 0.026	
vs. rim^{rescue}/rim^{R915H}		0.18		>0.9999
vs. rim^{R915H}/rim^{R915H}		<0.0001		>0.9999
rim^{rescue}/rim^{R915H} (*n* = 12 NMJs from 6 larvae)	44.80 ± 3.269		1.089 ± 0.029	
vs. rim^{R915H}/rim^{R915H}		0.0333		>0.9999
rim^{R915H}/rim^{R915H} (*n* = 24 NMJs from 17 larvae)	54.90 ± 2.472		1.056 ± 0.017	

Numerical values not stated in text or figure legends including p-values and sample sizes for measurements shown in Figure 2. PPR = paired pulse ratio, IPI = interpulse interval.

Supplementary Table 3 Data summary and statistical information of TEVC and focal recordings of RIM-overexpression constructs. Related to Figure 3.

TEVC parameter median (25th – 75th percentile)	*ok6-GAL4 > UAS-RIM^{wt}*	*ok6-GAL4 > UAS-RIM$^{R>H}$*	*P*-value
1.0 mM $[Ca^{2+}]_{EZR}$			
eEPSC amplitude [nA]	29.10 (22.30-42.75)	57.94 (46.68-68.34)	0.004
n (NMJs, animals)	11, 11	11, 11	
mEPSC amplitude [nA]	0.910 (0.808-1.095)	0.945 (0.813-1.083)	0.713
mEPSC rise time [ms]	0.800 (0.800-0.925)	0.900 (0.800-1.100)	0.114
mEPSC frequency [ms]	2.310 (1.738-3.645)	3.225 (1.583-3.968)	0.613
n (NMJs, animals)	14, 14	14, 14	

Focal recordings parameter median (25th – 75th percentile)	*ok6-GAL4 > UAS-RIM^{wt}*	*ok6-GAL4 > UAS-RIM$^{R>H}$*	*P*-value
1.0 mM $[Ca^{2+}]_{EZR}$			
eEPSC amplitude [nA]	1.59 (1.14-1.95)	3.23 (1.70-4.79)	0.008
eEPSC delay time [ms]	1.400 (1.225-1.488)	1.150 (1.050-1.400)	0.037
eEPSC rise time [ms]	0.856 (0.828-1.090)	0.690 (0.676-0.823)	0.012
eEPSC tau decay time [ms]	4.33 (3.60-4.66)	3.21 (2.75-3.71)	0.027
n (NMJs, animals)	11, 11	10, 10	

Focal recordings parameter median (25th – 75th percentile)	*ok6-GAL4 > UAS-RIM^{wt}*	*ok6-GAL4 > UAS-RIM$^{R>H}$*	*P*-value
0.5 mM $[Ca^{2+}]_{EZR}$			
eEPSC amplitude [nA]	2.05 (1.62-3.14)	1.71 (1.09-2.54)	0.372
eEPSC delay time [ms]	1.4 (1.337-1.462)	1.5 (1.350-1.613)	0.240
eEPSC rise time [ms]	1.07 (1.01-1.11)	1.07 (1.01-1.11)	0.999
eEPSC tau decay time [ms]	4.87 (4.48-5.38)	5.15 (4.13-5.28)	0.860
n (NMJs, animals)	6, 3	6, 3	

Numerical values not stated in text or figure legends including p-values and sample sizes for measurements with motoneuron-specific expression of *RIM^{wt}* (*ok6-GAL4 > UAS-RIM^{wt}*) and *RIM$^{R>H}$* (*ok6-GAL4 > UAS-RIM$^{R>H}$*) shown in Figure 3.

Supplementary Table 4 Data summary and statistical information of AZ morphology in larvae overexpressing RIM variants. Related to Figure 4.

Parameter median (25^{th} – 75^{th} percentile)	*ok6-GAL4 > UAS-RIM^{wt}*	*ok6-GAL4 > UAS-RIM$^{R>H}$*	*P*-value
confocal data			
Brp puncta / NMJ	541 (393-596)	539 (351-679)	0.914^{t}
NMJ size [μm^2]	573.812 (444.969-710.532)	748.684 (483.197-1086.828)	0.167^{t}
no. of boutons per NMJ	137 (93-159)	140 (96-158)	0.806^{t}
n (NMJs, animals)	17, 5	17, 5	
***d*STORM data**			
AZ area [μm^2]	0.086 (0.057-0.132)	0.087 (0.057-0.129)	0.812^{rs}
Brp locs. per AZ	1305 (844-2144)	1270 (852-2066)	0.632^{rs}
Brp loc. density [$10^4/\mu m^2$]	1.508 (1.201-1.907)	1.519 (1.218-1.843)	0.829^{rs}
n (AZs, NMJs, animals)	591, 15, 4	712, 15, 4	

Numerical values not stated in text or figure legends including p-values and sample sizes for measurements with motoneuron-specific expression of *RIM^{wt}* (*ok6-GAL4 > UAS-RIM^{wt}*) and *RIM$^{R>H}$* (*ok6-GAL4 > UAS-RIM$^{R>H}$*) shown in Figure 4. Statistical test used for comparison is indicated for each p-value with ^{t} = parametric t-test and ^{rs} = non-parametric rank sum test.

Supplementary Table 5 Data summary and statistical information of Ca^{2+} transients and BAPTA measurements in *RIM*^{wt} and *RIM*$^{R>H}$. Related to Figure 5.

Parameter median (25th – 75th percentile)	*ok6-GAL4 > UAS-RIM*^{wt}	*ok6-GAL4 > UAS-RIM*$^{R>H}$	*P*-value
ΔF/F	0.462 (0.347-0.663)	0.616 (0.346-0.685)	0.341
F baseline [AD-values]	693.334 (416.509-1168.890)	767.715 (407.559-1157.262)	0.862
Tau decay [ms]	0.083 (0.078-0.089)	0.116 (0.060-0.150)	0.139
n (boutons, NMJs, animals)	28, 10, 9	36, 10, 7	
normalized eEPSC amplitude reduction [nA]	0.210 (0.163-0.298)	0.380 (0.22-0.560)	0.006
n (boutons, NMJs, animals)	22, 12, 6	21, 14, 7	
normalized eEPSC PPR increase	1.464 (1.351-1.639)	1.188 (0.946-1.434)	0.002
n (boutons, NMJs, animals)	22, 12, 6	21, 16, 6	

Numerical values not stated in text or figure legends including p-values and sample sizes for measurements with motoneuron-specific expression of *RIM*^{wt} (*ok6-GAL4 > UAS-RIM*^{wt}) and *RIM*$^{R>H}$ *(ok6-GAL4 > UAS-RIM*$^{R>H}$) shown in Figure 5.

Supplementary Table 6. Data summary and statistical information of AZ morphology in RIM-CRISPR/Cas9 constructs. Related to Figure 6.

Parameter median (25th – 75th percentile)	*rim*^{rescue}/*rim*^{rescue}	*rim*$^{R>H}$/*rim*^{rescue}	*rim*$^{R>H}$/*rim*$^{R>H}$
confocal data			
Brp puncta / NMJ	536 (375-580)	634 (507-728)	701 (548-764)
p vs. *rim*^{rescue}/*rim*^{rescue}		0.075	0.008
NMJ size [µm^2]	570.873 (490.488-787.649)	865.870 (668.837-937.458)	751.125 (640.979-832.716)
p vs. *rim*^{rescue}/*rim*^{rescue}		0.045	0.999
no. of boutons per NMJ	99 (79-117)	123 (104-136)	148 (119-182)
p vs. *rim*^{rescue}/*rim*^{rescue}		0.124	< 0.001
n (NMJs, animals)	19, 7	16, 7	18, 6
dSTORM data			
*d*STORM AZ area [µm^2]	0.097 (0.072-0.144)	0.102 (0.071-0.150)	0.0930 (0.066-0.135)
p vs. *rim*^{rescue}/*rim*^{rescue}		0.990	0.058
Brp locs. per AZ	1755 (1148-2695)	1824 (1156-2854)	1613 (1049-2591)
p vs. *rim*^{rescue}/*rim*^{rescue}		0.990	0.112
Brp loc. density [10^4/µm^2]	1.709 (1.444-2.067)	1.756 (1.459-2.101)	1.719 (1.384-2.129)
p vs. *rim*^{rescue}/*rim*^{rescue}		0.990	0.990
n (AZs, NMJs, animals)	1088, 17, 6	898, 17, 6	855, 16, 6

Numerical values including p-values and sample sizes for confocal and *d*STORM measurements in flies carrying *rim* alleles (*rim*^{rescue}/*rim*^{rescue}, *rim*$^{R>H}$/*rim*^{rescue} and *rim*$^{R>H}$/*rim*$^{R>H}$) generated with CRISPR/Cas9 as shown in Figure 6. Anova on Ranks was used for statistical testing.